

# When Detectors Forget Forensics: Blocking Semantic Shortcuts for Generalizable AI-Generated Image Detection

Chao Shuai<sup>1</sup> Zhenguang Liu<sup>1</sup> Shaojing Fan<sup>2</sup> Bin Gong<sup>1</sup> Weichen Lian<sup>1</sup> Xiuli Bi<sup>3</sup> Zhongjie Ba<sup>1</sup> Kui Ren<sup>1</sup>

## Abstract

AI-generated image detection has become increasingly important with the rapid advancement of generative AI. However, detectors built on Vision Foundation Models (VFMs, *e.g.*, CLIP) often struggle to generalize to images created using unseen generation pipelines. We identify, for the first time, a key failure mechanism, termed *semantic fallback*, where VFM-based detectors rely on dominant pre-trained semantic priors (such as identity) rather than forgery-specific traces under distribution shifts. To address this issue, we propose **Geometric Semantic Decoupling (GSD)**, a parameter-free module that explicitly removes semantic components from learned representations by leveraging a frozen VFM as a semantic guide with a trainable VFM as an artifact detector. GSD estimates semantic directions from batch-wise statistics and projects them out via a geometric constraint, forcing the artifact detector to rely on semantic-invariant forensic evidence. Extensive experiments demonstrate that our method consistently outperforms state-of-the-art approaches, achieving 94.4% video-level AUC (+1.2%) in cross-dataset evaluation, improving robustness to unseen manipulations (+3.0% on DF40), and generalizing beyond faces to the detection of synthetic images of general scenes, including UniversalFakeDetect (+0.9%) and GenImage (+1.7%).

## 1. Introduction

The recent rise of advanced generative AI (Midjourney, 2022; Rombach et al., 2022) has raised serious questions about the authenticity of digital content, making it increasingly difficult to tell what is real and what is artificially generated. This technological leap has transitioned from a security risk to a driver of tangible, high-stakes catastrophes.

<sup>1</sup>Zhejiang University <sup>2</sup>National University of Singapore  
<sup>3</sup>Chongqing University of Posts and Telecommunications. Correspondence to: Zhenguang Liu <liuzhenguang2008@gmail.com>.

Preprint.

Recent incidents involving deepfake-based corporate scams and privacy violations underscore the fragility of the current digital ecosystem (Business, 2024; Brown, 2024). The rampant spread of such AI-generated content fosters a climate of universal skepticism, threatening the evidentiary value of all media. Addressing this challenge requires the engineering of an adaptive detection mechanism that remains effective against rapidly advancing synthesis techniques.

In response, the digital forensic community has undergone a significant methodological shift, moving beyond early statistical artifact analysis to data-driven deep learning paradigms. A consensus has emerged among state-of-the-art detectors (Yan et al., 2024b; Chen et al.; Li et al., 2025; Han et al., 2025; Cai et al., 2025; Yan et al., 2025), which mainly leverage large-scale pre-trained Vision Foundation Models (VFMs), such as CLIP (Radford et al., 2021). These models provide robust feature representations that have significantly boosted detection accuracy on standard benchmarks. However, a persistent paradox remains: while these detectors achieve near-perfect performance on seen training distributions, they suffer from catastrophic performance degradation when exposed to unseen generation techniques (Xie et al., 2025; Wang et al., 2024; Chen et al.). In this work, we posit that this failure stems from a fundamental conflict between the semantic-centric objective of pre-training and the artifact-centric objective of forensics. Consistent with observations (Yan et al., 2024b), semantic priors learned by foundation models concentrate in dominant representational directions, whereas transferable forensic artifacts reside in weaker, more domain-sensitive subspaces.

*We hypothesize that when forensic artifacts are subtle or exhibit poor transferability, the model falls back on the strong semantic priors (e.g., identity) embedded in the foundation model, overshadowing the faint signals of manipulation.* Motivated by this hypothesis, we diagnose the generalization bottleneck in vision transformer-based deepfake detectors by comparing feature distributions between frozen pre-trained CLIP and a fully fine-tuned counterpart using t-SNE (Maaten & Hinton, 2008) (Figure 1). We summarize four key observations:

**Observation I: Asymmetric Feature Distribution in Source Domain.** On the in-domain FaceForensics++ (Rossler

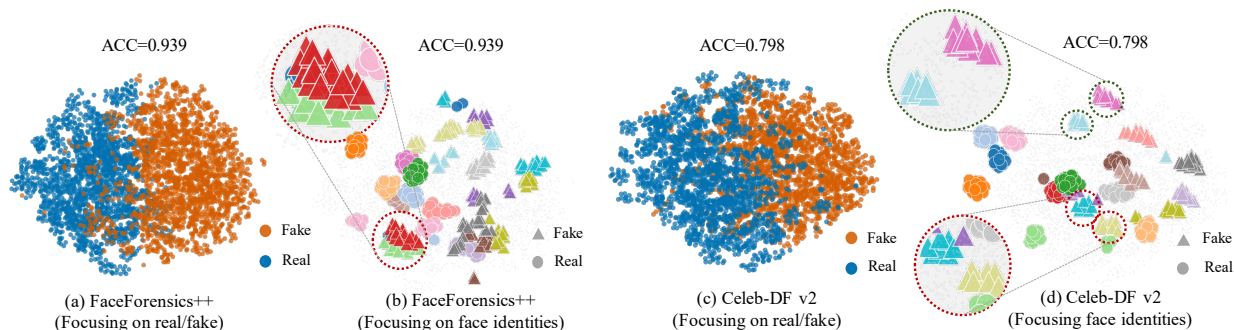


Figure 1. t-SNE (Maaten & Hinton, 2008) visualization of feature distributions extracted by the fine-tuned CLIP encoder on in-domain (FaceForensics++) and cross-domain (CelebDF-v2) datasets. Points are colored by forgery labels (a, c) and face identities (b, d); only 20 identities for clarity. On FaceForensics++ (a, b), real samples form tight identity-centric clusters, while fake samples exhibit clear identity-separated clusters, suggesting that learned forgery artifacts act as a repulsive forensic signal. When transferring to CelebDF-v2 (c, d), this semantic fallback becomes pervasive: due to the poor cross-domain transferability of learned forensic cues, a substantial fraction of fake samples almost re-aggregate by identity (e.g., green dashed circles), leading to increased overlap with real samples and reduced real/fake separability. Hard-to-separate samples (e.g., red dashed circles) likewise concentrate within cohesive identity clusters.

et al., 2019) test set (Figure 1(a) and (b)), despite the clear real/fake separation, the feature space exhibits a distinct asymmetry in clustering behavior. Real samples maintain tight, compact clusters corresponding to subject identities, indicating that the representation remains dominated by identity cues when forensic evidence is weak. Conversely, fake samples form multiple identity-separated clusters with looser and more scattered structure than real samples. This suggests that, although some identity structure persists, forgery-specific cues contribute additional discriminative variation that supports reliable real/fake discrimination.

**Observation II: Semantic Fallback and Feature Collapse.** When generalizing to the unseen Celeb-DF v2 (Li et al., 2020b) domain (Figure 1(c) and (d)), the model’s performance degrades significantly. Crucially, the feature space exhibits *semantic degeneration*: the discriminative power of learned forensic cues is substantially weakened, and the representation becomes increasingly dominated by pre-trained semantic priors. *Notably, as highlighted by the green dashed circles in Figure 1(d), a substantial fraction of fake samples re-aggregate into clusters organized by face identity.* Unlike the dispersed distribution in the source domain, these cross-domain deepfakes collapse back into the semantic manifold, resulting in markedly reduced separability.

**Observation III: Semantic Entanglement in Hard Examples.** We further analyze *hard samples* that remain inseparable in the binary classification space (indicated by the **red dashed circles**). By tracing these entangled regions to the identity-colored plots, we find that they consistently correspond to highly cohesive semantic clusters. This correlation strongly suggests that semantic dominance is the root cause of generalization failure: when the forensic signal is weak or unknown, the strong semantic consistency between a real image and its deepfake variant overshadows the subtle

forgery traces. See Appendix F.1 for other dataset analyses.

These observations align with a feature-collapse phenomenon under cross-domain shifts (Geirhos et al., 2020; Dong et al., 2023): the representation suppresses forgery-specific cues and instead over-relies on the strong semantic priors inherited from large-scale pretraining.

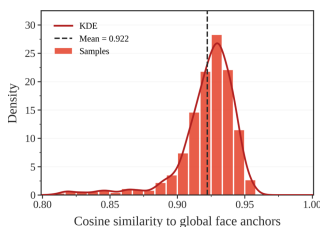


Figure 2. Analysis of Semantic Consistency. The distribution of cosine similarities between random samples and the global semantic anchor.

Motivated by these observations, we propose a **parameter-free Geometric Semantic Decoupling (GSD)**, which constrains the detector to learn within the **semantic null space**, a subspace mathematically orthogonal to the dominant semantic priors. Specifically, within each training mini-batch, we dynamically distill a **visual semantic consensus**, mathematically represented as the feature centroid of the frozen semantic anchor’s outputs. The validity of this consensus is corroborated by our analysis in Figure 2, where the high cosine similarity between random samples from FaceForensics++ and the global semantic centroid supports the existence of intrinsic consensus features. To construct the subspace spanning these semantic priors, we center all batch features around the centroid and apply QR decomposition (Gander, 1980) to obtain a set of orthogonal basis vectors. This process effectively estimates the dominant semantic directions specific to the current batch without requiring external reference data. Subsequently, we project the trainable detector’s features

represented as the feature centroid of the frozen semantic anchor’s outputs. The validity of this consensus is corroborated by our analysis in Figure 2, where the high cosine similarity between random samples from FaceForensics++ and the global semantic centroid supports the existence of intrinsic consensus features. To construct the subspace spanning these semantic priors, we center all batch features around the centroid and apply QR decomposition (Gander, 1980) to obtain a set of orthogonal basis vectors. This process effectively estimates the dominant semantic directions specific to the current batch without requiring external reference data. Subsequently, we project the trainable detector’s features

onto this basis to isolate the semantic component. Finally, we explicitly subtract this semantic vector from the original features, thereby preserving forensic artifacts residing in the orthogonal complement. Unlike the baseline which succumbs to identity-based clustering, the GSD-enhanced detector constructs a feature space where forensic separability is dominant, effectively eliminating the *semantic fallback* (see Figure 3). In summary, our main contributions are:

- We identify *semantic fallback* as the **root cause** of generalization failure, wherein VFM-based detectors regress to pre-trained semantic priors (*e.g.*, identity cues) when deployed in unseen domains. Importantly, we show that this failure mode is not arbitrary: the dominant semantic subspace is highly structured and stable. As a result, it can be reliably estimated by distilling a *visual semantic consensus* directly from batch-wise statistics, eliminating the need for optimization constraints or complex module designs.
- Building on this insight, we introduce **Geometric Semantic Decoupling (GSD)**, a **parameter-free** module that **geometrically removes dominant semantic components** from learned representations, thereby preventing identity-based shortcut learning, allowing the model to focus on manipulation-specific forensic signals rather than semantic identity cues. Unlike prior approaches that rely on auxiliary losses or architectural complexity, GSD directly estimates a *semantic consensus* from batch-wise statistics and constructs an explicit semantic basis via QR decomposition.
- We conduct extensive evaluations across diverse benchmarks, showing that our method consistently outperforms state-of-the-art approaches. In particular, it achieves +1.2% video-level AUC on challenging cross-dataset evaluations and +3.0% video-level AUC on unseen manipulation scenarios, demonstrating strong generalization from known facial deepfakes to unseen manipulations. Importantly, this generalization extends beyond faces to AI-generated images of general scenes, where our method sets new state-of-the-art results on UniversalFakeDetect (+0.9%) and GenImage (+1.7%).

## 2. Related work

In this section, we focus on the works most directly relevant to our approach. For a comprehensive review of the related literature, please refer to Appendix C.

**Generalizable AI-generated Image Detection.** Driven by the remarkable generalization capabilities of large-scale pre-training, recent research has pivoted toward leveraging Vision Foundation Models (VFMs), such as CLIP (Radford et al., 2021), as primary backbones. Prominent approaches, including Forensics Adapter (Cui et al., 2025),

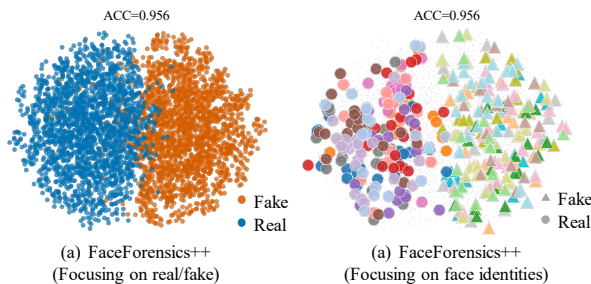


Figure 3. t-SNE visualization of features extracted by the fine-tuned CLIP augmented with the Geometric Semantic Decoupling (GSD) module. Points are colored by forgery labels (a) and face identities (b). Notably, the features exhibit a clear real/fake separation and preserves pronounced identity-separated clusters, indicating that the model primarily relies on forgery-specific features.

FatFormer (Liu et al., 2024a), C2P-CLIP (Tan et al., 2025), CLIPMoLE (Liu et al., 2024b) and LGrad (Tan et al., 2023) leverage parameter-efficient paradigms (*e.g.*, adapters, LoRA (Hu et al., 2022), and prompt learning) to align generic features with forensic cues. Furthermore, the emergent wave of Multimodal Large Language Models (MLLMs) integrates visual encoders with LLMs to facilitate interpretable, reasoning-driven detection (Chen et al.; Xu et al., 2024). However, a critical side effect of this paradigm is that VFMs are inherently optimized for semantic alignment. This creates a fundamental conflict: the backbone’s strong bias toward high-level semantics (*e.g.*, identity) can overshadow the subtle, low-level artifacts required for effective forgery detection, necessitating explicit mechanisms to suppress this semantic dominance. In this work, we address this challenge by introducing a geometry-driven, parameter-free decoupling mechanism that explicitly removes dominant semantic components from VFM representations, enabling robust and generalizable AI-generated image detection without compromising forensic sensitivity.

**Disentanglement and Semantic Debiasing.** Some studies aim to disentangle forensic cues from confounding factors such as identity and background content. For instance, prior works (Cao et al., 2022; Luo et al., 2023; Ba et al., 2024; Yan et al., 2023a) introduce explicit constraints and disentanglement objectives to learn forgery-invariant representation. Besides, UDD (Fu et al., 2025) disrupts semantic dependencies by shuffling transformer tokens, forcing the network to focus on forgery traces. UCF (Yan et al., 2023a) suppresses semantic information by employing a dedicated content reconstruction branch to absorb high-level features, thereby attempting to distill the forensic branch. Effort (Yan et al., 2024b) utilize singular value decomposition (SVD) to construct orthogonality constraints for preserving pre-trained knowledge, while diffusion priors have also been employed to guide models toward manipulation-consistent cues (Sun et al., 2024). However, these approaches typically rely on

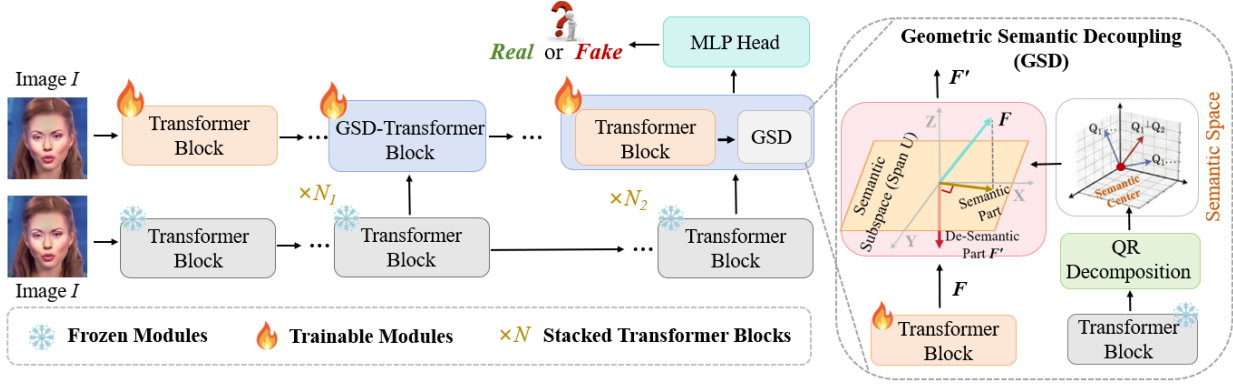


Figure 4. Overview of the proposed **Geometric Semantic Decoupling (GSD)** framework. GSD adopts an asymmetric dual-stream architecture consisting of a frozen semantic basis extractor (bottom) and a trainable artifact detector (top). **Unlike prior parameter-efficient adaptations**, we estimate a **dynamic semantic basis**  $U$  directly from batch-wise statistics via Householder-based QR decomposition, where  $\text{span}(U)$  characterizes the dominant semantic manifold encoded by the frozen backbone. The GSD module then enforces an explicit **geometric constraint** by projecting learnable intermediate detector features  $F$  onto the orthogonal complement of the estimated semantic subspace. This **parameter-free semantic subtraction** removes the semantic component  $F^{\parallel}$  and yields de-semanticized features  $F'$ , compelling the detector to rely solely on generalizable forensic artifacts rather than semantic shortcuts.

learnable auxiliary parameters or soft optimization objectives to suppress semantics, which may still allow semantic leakage when facing strong domain shifts. In contrast, our approach introduces a parameter-free Geometric Semantic Decoupling (GSD) mechanism. Instead of implicitly learning to disentangle, we impose a geometric constraint by explicitly projecting features onto the semantic null space.

### 3. Methodology

Motivated by the observation that semantic fallback is a key confounder for cross-domain deepfake detection, we propose **Geometric Semantic Decoupling (GSD)**, a parameter-free module that decouples forensic cues from semantic content. As shown in Figure 4, GSD has two parallel streams: (i) a frozen semantic extractor that estimates a batch-induced semantic subspace, and (ii) a trainable artifact detector constrained to its orthogonal complement.

#### 3.1. Dynamic Semantic Basis Construction

We introduce a strategy to distill a semantic consensus directly from batch-wise statistics. Let  $\mathcal{B} = \{x_1, \dots, x_B\}$  denote the current training mini-batch containing  $B$  images, and  $g_i \in \mathbb{R}^D$  be the global feature vector extracted by the frozen VFM for image  $I_i$ . We first compute the semantic anchor  $c$  of the current batch:

$$c = \frac{1}{B} \sum_{i=1}^B g_i. \quad (1)$$

We posit that  $c$  encapsulates the common visual structures shared by the batch.

To derive a dynamic semantic basis  $U \in \mathbb{R}^{D \times K}$  that spans

the dominant semantic manifold, we perform a QR decomposition on the centered feature variations. In practice, we utilize the Householder-based QR decomposition (Dass & Mahapatra, 2021) for superior numerical stability. Specifically, we construct the centered guide matrix  $G = [v_1, \dots, v_B] \in \mathbb{R}^{D \times B}$ , where  $v_i = g_i - c$ . The orthonormal factor  $Q$  is obtained through a sequence of Householder reflections. At each step  $t$ , we define  $z^{(t)} = A_{t:D, t}^{(t)} \in \mathbb{R}^{D-t+1}$  as the  $t$ -th column subvector of the remaining submatrix  $A^{(t)}$ .

We construct the Householder vector  $u^{(t)} = z^{(t)} + \alpha^{(t)} e_1$ , where  $\alpha^{(t)} = \text{sign}(z_1^{(t)}) \|z^{(t)}\|_2$ . By normalizing  $u^{(t)}$  as  $w^{(t)} = u^{(t)} / \|u^{(t)}\|_2$ , the reflector is given by:

$$H^{(t)} = I - 2w^{(t)}w^{(t)\top}. \quad (2)$$

The decomposition yields the upper-triangular factor  $R = H^{(T)} \dots H^{(1)} G$  and the orthonormal factor  $Q = H^{(1)} \dots H^{(T)}$ . Finally, we define the **dynamic semantic basis** as the first  $K$  columns of  $Q$ :

$$U = Q_{[:, 1:K]} \in \mathbb{R}^{D \times K}, \quad K \leq \text{rank}(G). \quad (3)$$

$\text{Span}(U)$  captures the instantaneous semantic subspace induced by the current mini-batch. Crucially,  $U$  is re-estimated for every iteration, ensuring the semantic removal is adaptively aligned with the current data distribution.

#### 3.2. Geometric Semantic Decoupling

The GSD module is integrated into the deeper layers of the trainable artifact detector. Let  $F_l \in \mathbb{R}^{N \times D}$  denote the input token sequence (excluding the [CLS] token) for the  $l$ -th Transformer block. We first project the detector's features

onto the dynamic semantic basis  $U$  to identify the semantic component:

$$F_l^{\parallel} = F_l U U^{\top}. \quad (4)$$

$F_l^{\parallel}$  represents the projection of the trainable features onto the subspace spanned by the frozen semantic priors. To eliminate *semantic fallback*, we subtract this component, effectively projecting  $F_l$  onto the semantic null space. The resulting de-semantic features  $F_l'$  are computed as:

$$F_l' = F_l - F_l^{\parallel} = F_l(I - U U^{\top}), \quad (5)$$

where  $I \in \mathbb{R}^{D \times D}$  is the identity matrix. By construction, Equation 5 ensures that  $F_l'$  is mathematically orthogonal to the semantic priors ( $\langle F_l', \mathbf{u}_k \rangle = 0$ ), forcing the detector to rely on forensic artifacts residing in the null space.

### 3.3. Training Objective

The GSD mechanism imposes a hard structural constraint, obviating the need for complex auxiliary disentanglement losses. The detector is trained end-to-end using the standard Binary Cross-Entropy (BCE) loss:

$$\mathcal{L} = -\mathbb{E}_{(x,y) \sim \mathcal{D}} [y \log(f(x)) + (1-y) \log(1-f(x))], \quad (6)$$

where  $f(x) = \mathcal{C}(\Phi_{\text{det}}(x))$  represents the probability prediction. Here,  $\Phi_{\text{det}}(\cdot)$  denotes the trainable detector backbone that produces the purified features, and  $\mathcal{C}(\cdot)$  is the subsequent classification head.

## 4. Experiments

### 4.1. Implementation Details

We adopt the pre-trained **CLIP ViT-L/14** (Radford et al., 2021) as our visual backbone. The network is optimized end-to-end using the AdamW (Loshchilov & Hutter, 2017) optimizer, with a learning rate set to  $1 \times 10^{-6}$  for the backbone and a batch size of 128. All experiments are conducted on NVIDIA A100 GPUs. To simulate real-world degradation, we incorporate standard data augmentations, including Gaussian blur and JPEG compression, following the protocol in (Yan et al., 2024a; 2023b). Regarding the proposed Geometric Semantic Decoupling (GSD) module, we inject it into the final 4 layers of the CLIP encoder by default. We defaultly set the number of orthogonal basis vectors ( $K$ ) to 16. We provide detailed ablation studies analyzing the impact of different insertion depths and subspace dimensions in Table 4, respectively. We report Video-level AUC, Frame-level AUC, and Accuracy (ACC).

We consider two evaluation regimes: face forgery detection and synthetic image detection. **Face forgery detection:** We adopt FaceForensics++ (FF++) (Rossler et al., 2019) as the source domain for training, using the High-Quality

compression setting (c23) following DeepfakeBench (Yan et al., 2023b). We evaluate generalization along two axes: **(i) cross-dataset generalization**, where models trained on FF++ are directly tested on multiple unseen target datasets; and **(ii) cross-manipulation generalization**, where we test on DF40 (Yan et al., 2024c) with six representative forgery types. **Synthetic image detection:** We additionally benchmark on UniversalFakeDetect (Ojha et al., 2023) and GenImage (Zhu et al., 2023), and follow the training/evaluation protocols in (Ojha et al., 2023; Zhu et al., 2023). Full dataset lists and generator details are provided in Appendix A.1.

To provide a comprehensive benchmark, we evaluate against a broad set of competitive detectors spanning three families: **(i) foundation baselines** (e.g., Efficient-b4 (Tan & Le, 2019), and CLIP (Radford et al., 2021)), **(ii) face-forgery detectors** (e.g., F3Net (Qian et al., 2020), SBIs (Shiohara & Yamasaki, 2022), and recent robust models such as Effort (Yan et al., 2024b)), and **(iii) synthetic-image detectors** (e.g., UniFD (Ojha et al., 2023), C2P (Tan et al., 2025), and MPFT (Niu et al., 2026)). More details are in Appendix A.2.

### 4.2. Face Forgery Detection

**Cross-Dataset Generalization Results.** To evaluate robustness against unknown domains, we benchmark our model on five distinct datasets after training solely on FF++. As detailed in Table 1, the proposed GSD establishes a new state-of-the-art standard. In terms of Video-level AUC, our method achieves a remarkable average of **94.4%**, surpassing the strongest competitor ForAda (Cui et al., 2025), by a substantial margin of **+1.2%**. Notably, on the challenging DFDC benchmark, where most priors struggle, GSD improves performance from 85.3% to **88.3%**, validating that our geometric decoupling strategy effectively mitigates semantic interference in complex scenes. A similar trend is observed in Frame-level AUC, where GSD attains an average of **90.3%**, outperforming the previous best result (GM-DF (Lai et al., 2025), 88.2%) by **2.1%**.

**Cross-Manipulation Generalization Results.** We further assess the model’s ability to generalize across unknown forgery techniques using the DF40 dataset. As shown in Table 2, we evaluate performance on six representative face-swapping methods. The results demonstrate the superior stability of GSD. Our method achieves an average Video-level AUC of **97.8%**, consistently outperforming recent state-of-the-art models like Effort (Yan et al., 2024b) and VbSaT (Yan et al., 2025) (both at 94.8%) by **+3.0%**. More impressively, in the fine-grained frame-level evaluation, GSD reaches an average AUC of **94.5%**, exceeding the runner-up (FSgD (Ma et al., 2025), 87.8%) by a significant **+6.7%**. This confirms that by strictly learning within the semantic null space, GSD captures intrinsic forensic artifacts that are invariant across different generation algorithms.

Table 1. Our method outperforms existing approaches in both video-level and frame-level AUC (%) on cross-datasets. “–” indicates that the corresponding results are not reported in the original paper, and † indicates that the results are obtained by using the official pre-trained model or reproduction, and the remaining results are cited from (Yan et al., 2024b; Chen et al.) and the original paper.

Methods	Video-level AUC						Methods	Frame-level AUC					
	CDF-v2	CDF-v1	DFDC	DFDCP	DFD	Avg.		CDF-v2	CDF-v1	DFDC	DFDCP	DFD	Avg.
F3Net (ECCV’20)	78.9	–	71.8	74.9	84.4	77.5	Efficient-b4† (ICML’19)	74.9	70.5	69.6	72.8	81.5	73.9
CLIP† (ICML’21)	88.4	89.6	83.3	86.3	92.6	88.0	CLIP† (ICML’21)	83.2	86.1	80.7	82.4	87.7	84.0
LaV (MM’23)	92.2	84.7	82.0	89.7	96.8	89.1	Face X-Ray (CVPR’20)	67.9	70.9	63.3	69.4	76.7	69.6
IID (CVPR’23)	83.8	–	70.0	68.9	93.9	79.2	RECCE (CVPR’22)	73.2	–	71.3	74.2	74.2	73.2
CFM (TIFS’23)	89.7	–	70.6	80.2	95.2	83.9	UCF† (ICCV’23)	82.4	77.9	80.5	75.9	87.8	80.9
SbIs (CVPR’22)	90.6	–	75.2	87.7	88.2	85.4	ICT (CVPR’23)	85.7	81.4	–	–	84.1	83.7
ProDe† (NeurIPS’24)	92.6	95.7	70.7	82.8	95.4	87.4	ProDe† (NeurIPS’24)	84.5	90.9	72.4	81.2	–	82.3
CDFa† (ECCV’24)	93.8	92.1	83.0	88.1	95.4	90.5	DFFake (NeurIPS’24)	80.5	–	–	81.0	90.4	84.0
FakeRadar (ICCV’25)	91.7	–	84.1	88.5	96.2	90.1	ExposDe† (AAAI’24)	86.4	81.8	72.1	85.1	89.8	83.0
VbSaT (CVPR’25)	94.7	–	84.3	90.9	96.5	91.6	DAID (NeurIPS’25)	84.4	–	66.9	–	91.2	80.8
DeepShield (ICCV’25)	92.2	–	82.8	93.2	96.1	91.1	UDD (AAAI’25)	86.9	–	75.8	85.6	91.0	84.8
FCG (CVPR’25)	95.0	–	81.8	–	–	88.4	FSgD (NeurIPS’25)	86.7	90.1	–	81.8	82.1	85.2
$\chi^2$ -DFD (NeurIPS’25)	95.5	–	85.3	91.2	95.7	91.9	LSDA (CVPR’24)	83.0	86.7	73.6	81.5	88.0	82.6
Effort† (ICML’25)	95.6	91.8	84.3	90.9	96.5	91.8	FreqDebias (CVPR’25)	83.6	87.5	74.1	82.4	86.8	82.9
ForAda (CVPR’25)	95.7	–	87.2	92.9	97.1	93.2	GM-DF (MM’25)	89.2	89.3	84.7	88.9	92.8	88.2
Ours	<b>96.4</b>	<b>96.4</b>	<b>88.3</b>	<b>93.2</b>	<b>97.7</b>	<b>94.4</b>	Ours	<b>90.6</b>	<b>91.0</b>	<b>85.5</b>	<b>89.9</b>	<b>94.3</b>	<b>90.3</b>

Table 2. Our method achieves superior video-level and frame-level AUC (%) on unseen manipulation methods. Results are reported on six representative face-swapping methods selected from DF40, where all samples are generated based on the FF++ domain. Top results are highlighted in **bold**.

Methods	Video-level AUC							Methods	Frame-level AUC						
	UniFace	e4s	FaceDancer	FSGAN	InSwap	SimSwap	Avg.		UniFace	e4s	FaceDancer	FSGAN	InSwap	SimSwap	Avg.
CLIP (ICML’21)	91.0	91.6	89.8	96.0	88.5	80.3	89.5	CLIP (ICML’21)	86.5	87.8	85.6	92.0	83.9	76.3	85.4
RECCE (CVPR’22)	89.8	68.3	84.8	94.9	84.8	76.8	83.2	RECCE (CVPR’22)	84.2	65.2	78.3	88.4	79.5	73.0	78.1
SBI (CVPR’22)	72.4	75.0	59.4	80.3	71.2	70.1	71.4	IID (CVPR’23)	79.5	71.0	79.0	86.4	74.4	64.0	75.7
UCF (ICCV’23)	83.1	73.1	86.2	93.7	80.9	64.7	80.3	SBI (CVPR’22)	64.4	69.0	44.7	87.9	63.3	56.8	64.4
IID (CVPR’23)	83.9	76.6	84.4	92.7	78.9	64.4	80.2	UCF (ICCV’23)	78.7	69.2	80.0	88.1	76.8	64.9	76.3
LSDA (CVPR’24)	87.2	69.4	72.1	93.9	85.5	69.3	79.6	LSDA (CVPR’24)	85.4	68.4	75.9	83.2	81.0	72.7	77.8
ProDe (NeurIPS’24)	90.8	77.1	74.7	92.8	83.7	84.4	83.9	CDFa (ECCV’24)	76.5	67.4	75.4	84.8	72.0	76.1	75.4
CDFa (ECCV’24)	76.2	63.1	80.3	94.2	77.2	75.7	77.8	ProDe (NeurIPS’24)	84.5	71.0	73.6	86.5	78.8	77.8	78.7
VbSaT (CVPR’25)	96.0	98.0	91.6	96.4	93.7	93.1	94.8	FSgD (NeurIPS’25)	91.8	87.5	83.0	86.3	87.4	<b>91.0</b>	87.8
Effort (ICML’25)	96.2	98.3	92.6	95.7	93.6	92.6	94.8	$\chi^2$ -DFD (NeurIPS’25)	85.2	91.2	83.8	89.9	78.4	84.9	85.6
Ours	<b>98.6</b>	<b>99.5</b>	<b>97.5</b>	<b>98.8</b>	<b>96.6</b>	<b>95.7</b>	<b>97.8</b>	Ours	<b>96.1</b>	<b>97.9</b>	<b>93.7</b>	<b>96.1</b>	<b>92.1</b>	<b>91.0</b>	<b>94.5</b>

### 4.3. Synthetic Image Detection

Following the protocol of (Ojha et al., 2023; Wang et al., 2020; Yan et al., 2024b), we train the detector using only ProGAN-generated (Karras et al., 2017) images and their real counterparts. As presented in Table 3, our method achieves a new state-of-the-art mean accuracy (mACC) of **96.1%**, surpassing the previous best method, Effort (Yan et al., 2024b) (95.2%), as well as other competitive approaches like MPFT (Niu et al., 2026) (94.6%) and C2P-CLIP (Tan et al., 2025) (93.8%). These results validate the effectiveness of our proposed framework in learning generalized features from a single source domain to detect unseen forgeries generated by diverse generators. To specifically evaluate our method on state-of-the-art diffusion-based generators, we further leverage the GenImage dataset, and the results of GenImage are reported in Appendix D.2.

### 4.4. Feature Analysis

To intuitively investigate how the proposed GSD module influences the internal representation of the foundation model, we visualize the self-attention maps of the [CLS] token from the last Transformer block. We compare the attention distributions across three settings: the frozen pretrained CLIP, the naively finetuned CLIP, and our CLIP w/ GSD. The visualization results are presented in Figure 5.

We summarize our observations as follows: **1) Attention collapse and semantic fallback.** Both the pretrained and naively finetuned CLIP exhibit a phenomenon known as attention collapse (Zhao et al., 2024), where attention excessively concentrates on sparse, single-pixel hotspots. **Crucially, the attention patterns of the finetuned CLIP are almost identical to those of the pretrained CLIP.** This empirical evidence supports our motivation that *even after fine-tuning, the learned representation can remain dominated*

Table 3. Our method achieves superior ACC (%) performance in cross-method evaluations on the UniversalFakeDetect Dataset. Following (Ojha et al., 2023), ProGAN is used for training, and others are used for testing. Some results of the compared methods are cited from (Yan et al., 2024b). The best results in each column are highlighted in **bold**.

Methods	GAN						Deep fakes	Low level		Perceptual loss		Guided	LDM			Glide			Dalle	mACC
	Pro-GAN	Cycle-GAN	Big-GAN	Style-GAN	Gau-GAN	Star-GAN		SITD	SAN	CRN	IMLE		200 steps	200 w/cfg	100 steps	100 27	50 27	100 10		
CNN-Spot (CVPR'20)	<b>100.0</b>	85.2	70.2	85.7	79.0	91.7	53.5	66.7	48.7	86.3	86.3	60.1	54.0	55.0	54.1	60.8	63.8	65.7	55.6	69.6
Patchfor (ECCV'20)	75.0	69.0	68.5	79.2	64.2	63.9	75.5	75.1	75.3	72.3	55.3	67.4	76.5	76.1	75.8	74.8	73.3	68.5	67.9	71.2
Co-occurrence (ArXiv'20)	97.7	63.1	53.8	92.5	51.1	54.7	57.1	63.1	55.9	65.7	65.8	60.5	70.7	70.5	71.0	70.2	69.6	69.9	67.5	66.9
Freq-spec (WIFS'20)	49.9	<b>99.9</b>	50.5	49.9	50.3	99.7	50.1	50.0	48.0	50.6	50.1	50.9	50.4	50.4	50.3	51.7	51.4	50.4	50.0	55.5
F3Net (ECCV'20)	99.4	76.4	65.3	92.6	58.1	<b>100.0</b>	63.5	54.2	47.3	51.5	51.5	69.2	68.2	75.3	68.8	81.7	83.2	83.0	66.3	71.3
CLIPf (ICML'21)	<b>100.0</b>	97.0	98.1	82.3	<b>100.0</b>	87.6	53.0	59.1	50.0	73.1	90.3	48.0	81.3	61.6	80.4	57.2	59.8	57.9	81.4	74.6
UniFD (CVPR'23)	<b>100.0</b>	98.5	94.5	82.0	99.5	97.0	66.6	63.0	57.5	59.5	72.0	70.0	94.2	73.8	94.4	79.1	79.8	78.1	86.8	81.4
LGrad (CVPR'23)	99.8	85.4	82.9	94.8	72.5	99.6	58.0	62.5	50.0	50.7	50.8	77.5	94.2	95.8	94.8	87.4	90.7	89.5	88.3	80.3
FreqNet (AAAI'24)	97.9	95.8	90.5	<b>97.5</b>	90.2	93.4	97.4	88.9	59.0	71.9	67.3	86.7	84.5	<b>99.6</b>	65.6	85.7	97.4	88.2	59.1	85.1
NPR (CVPR'24)	99.8	95.0	87.5	96.2	86.6	99.8	76.9	66.9	<b>98.6</b>	50.0	50.0	84.5	97.7	98.0	98.2	96.2	97.2	97.3	87.2	87.6
FatFormer (CVPR'24)	99.9	99.3	99.5	97.2	99.4	99.8	93.2	81.1	68.0	69.5	69.5	76.0	98.6	94.9	98.7	94.3	94.7	94.2	<b>98.8</b>	90.9
Effort (ICML'25)	<b>100.0</b>	99.8	<b>99.6</b>	95.0	99.6	<b>100.0</b>	87.6	92.5	81.5	98.9	98.9	69.2	99.3	96.8	<b>99.5</b>	<b>97.5</b>	<b>97.8</b>	97.2	98.0	95.2
C2P-CLIP (AAAI'25)	<b>100.0</b>	97.3	99.1	96.4	99.2	99.6	93.8	<b>95.6</b>	64.4	93.3	93.3	69.1	99.3	97.3	99.3	95.3	<b>95.3</b>	96.1	98.6	93.8
MPFT (Arxiv'26)	99.9	99.2	97.3	94.9	97.6	99.7	<b>97.6</b>	94.7	90.9	87.7	84.8	82.0	99.3	97.2	<b>99.5</b>	95.5	96.3	96.8	98.4	94.6
Ours	<b>100.0</b>	99.2	99.4	96.4	99.8	<b>100.0</b>	82.4	85.3	85.7	<b>99.0</b>	<b>99.2</b>	<b>90.8</b>	<b>99.4</b>	97.7	<b>99.5</b>	<b>97.5</b>	97.6	<b>97.6</b>	98.5	<b>96.1</b>

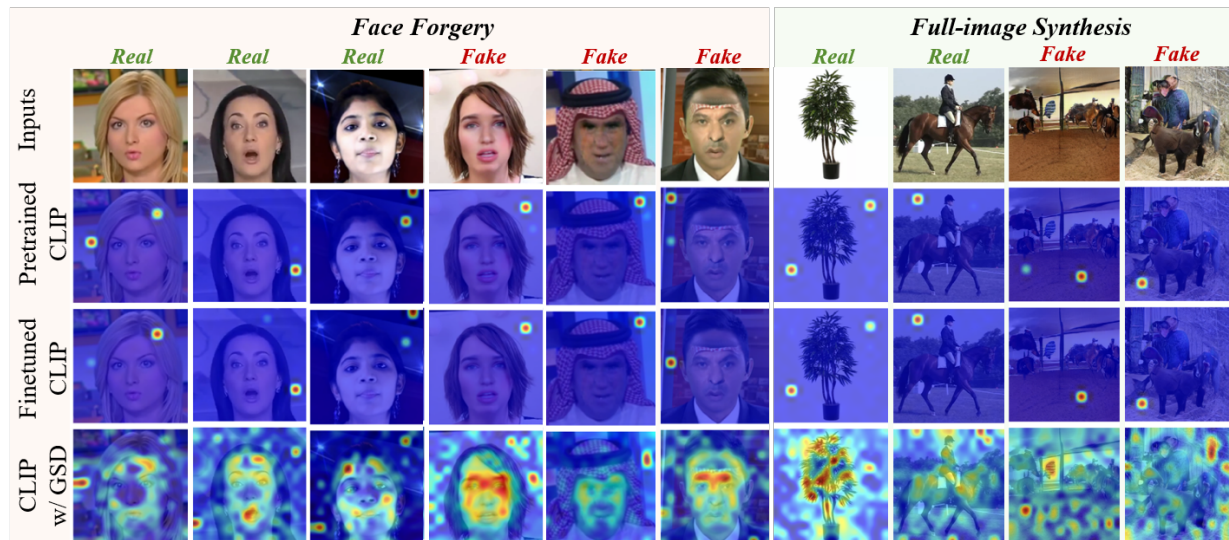


Figure 5. Visualization of self-attention maps. Pretrained and naively fine-tuned CLIP exhibit attention collapse with sparse hotspot patterns, and the fine-tuned model produces attention maps that are nearly identical to the pretrained one, suggesting a *semantic fallback* to strong foundation priors. In contrast, integrating GSD suppresses the dominance of semantic regions and shifts attention *toward forensic-relevant cues*: for real images, attention concentrates on blending edges and texture-rich regions, while for face-forgery images, it highlights manipulated regions; for synthetic images, attention becomes markedly less localized and spreads across the image.

by the strong semantic priors (e.g., face identity and object category) inherited from the pretrained foundation model, thereby suppressing weak and non-transferable forensic cues. **2) Semantic decoupling via GSD.** Upon integrating the GSD module, the model demonstrates a fundamental shift in its attention mechanism. As shown in the bottom row of Figure 5, GSD effectively suppresses the dominance of semantic features. Unlike the baselines, *our model does not fixate on semantic priors but instead redirects its focus toward forensic-relevant clues*. Remarkably, even without pixel-level supervision, our model learns to locate manipulation artifacts autonomously. For real images, the attention is distributed along *blending edges* and texture-rich regions,

which are critical regions for AI-generated image detection. For face-forgery images, attention concentrates on the manipulated regions, while for synthetic images, the attention maps become markedly less localized and spread across the image, *consistent with the fact that synthesis artifacts are distributed globally*. This confirms that GSD successfully guides the model toward a more robust, artifact-aware representation. More analyses are provided in Appendix F.2.

#### 4.5. Ablation Study

**The Impact of GSD Insertion Depth.** In hierarchical architectures (e.g., CLIP ViT-L/14), representations transition from low-level visual patterns in early layers to higher-level

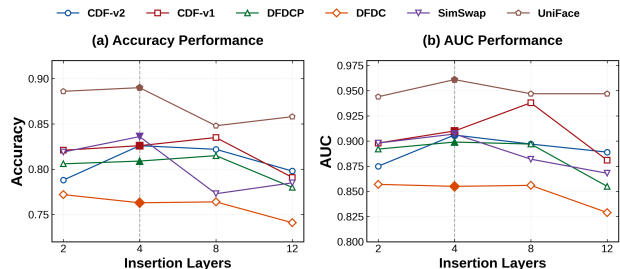


Figure 6. Ablation studies on GSD insertion positions within CLIP ViT-L/14 attention layers (ACC and Frame-level AUC).

Table 4. Ablation studies on  $K$  (frame-level AUC and ACC (%)). All models are trained on FF++ (c23) and evaluated on CDF-v1, CDF-v2, DFDCP, DFD, and DFDC.

$K$	Metric	CDF-v2	CDF-v1	DFDCP	DFD	DFDC
$K=2$	ACC	82.8	82.7	<b>81.2</b>	90.8	<b>77.1</b>
	AUC	90.1	90.4	89.1	94.1	85.8
$K=8$	ACC	82.6	<b>82.9</b>	80.7	90.9	76.7
	AUC	90.3	<b>92.0</b>	89.7	94.1	85.5
$K=16$	ACC	<b>83.5</b>	82.6	80.9	91.0	76.3
	AUC	90.6	91.0	89.9	<b>94.3</b>	85.5
$K=32$	ACC	83.3	82.8	80.2	90.4	76.7
	AUC	90.5	91.9	<b>90.0</b>	<b>94.3</b>	85.6
$K=64$	ACC	82.5	82.7	80.4	<b>91.2</b>	76.8
	AUC	<b>90.7</b>	90.9	89.9	<b>94.3</b>	<b>85.9</b>

semantic concepts in deeper layers. Therefore, the GSD insertion depth is critical for balancing semantic suppression and artifact preservation. We evaluate applying GSD to the last  $N$  Transformer blocks in Figure 6 and observe: 1) Extending GSD to include earlier layers (e.g.,  $N = 12$ ) leads to a clear performance drop, likely because these layers are dominated by low-level visual primitives; projecting them may inadvertently remove useful forensic cues such as texture irregularities and blending boundaries. 2) When restricting GSD to only the final 2 layers, we observe a slight performance decline compared to the peak at  $N = 4$ , suggesting that semantic decoupling benefits from a moderate depth to progressively refine the representation before classification. 3) The model achieves the best performance when GSD is applied to the last 4 layers, indicating that *semantic fallback* is largely a high-level phenomenon. Intervening at this depth effectively targets semantic abstractions, while preserving earlier accumulated forensic information.

### The Impact of Semantic Subspace Configuration $K$ .

We conduct an ablation study to determine the optimal dimensionality  $K$  of the estimated semantic subspace. The results are reported in Table 4. Remarkably, we observe that the detection performance is robust even with an extremely low-dimensional subspace constraint. Setting  $K = 2$  (i.e., utilizing only 2 orthogonal basis vectors) already yields highly competitive performance across all benchmarks (e.g., 90.1% AUC on CDF-v2). As  $K$  increases from 2 to 64, the

Table 5. Ablation on feature aggregation for semantic consensus: Global Average Pooling vs. [CLS] token.

Method	Metric	CDF-v2	CDF-v1	DFDCP	DFD
Avg-Pooling	ACC	<b>83.5</b>	<b>82.6</b>	<b>80.9</b>	<b>91.0</b>
	AUC	<b>90.6</b>	<b>91.0</b>	<b>89.9</b>	<b>94.3</b>
	Video-AUC	<b>96.4</b>	<b>96.4</b>	<b>93.2</b>	<b>97.7</b>
[CLS] Token	ACC	80.2	81.2	80.8	90.3
	AUC	89.2	88.8	88.7	<b>94.3</b>
	Video-AUC	94.6	95.3	92.7	97.5

performance gains are marginal. For instance, expanding the subspace dimension 32-fold (from  $K = 2$  to 64) yields less than a 1% improvement on most datasets (90.1% vs. 90.7% on CDF-v2). This empirical evidence corroborates our hypothesis that the *visual semantic consensus* within each dataset exhibits high semantic redundancy. The intrinsic semantic priors reside in a highly compact manifold, so a low-dimensional subspace spanned by a small set of orthogonal directions is sufficient to capture them.

**Feature Aggregation for Semantic Consensus.** We investigate the optimal strategy for distilling the visual semantic consensus. We compare using the Global Average Pooling (GAP) of patch tokens against the standard [CLS] token to compute the semantic centroid. As reported in Table 5, the GAP strategy consistently outperforms the [CLS] token across most benchmarks. For instance, GAP achieves a Video-level AUC of 96.4% on CDF-v2 and 98.8% on FSGAN, surpassing the [CLS] token by 1.8% and 0.3%, respectively. We think that GAP aggregates spatial information more uniformly across the image, yielding a more stable representation for the subsequent QR decomposition in the same patch-feature space. In contrast, the [CLS] token in CLIP is pre-trained to align with text and may emphasize salient regions. Since GSD is applied to the patch-level tokens (excluding the [CLS] token), this representation can be less well matched to the geometry of patch tokens.

## 5. Conclusions

In this paper, we identify a critical challenge in detecting AI-generated content: *semantic fallback*, a failure mechanism in VFM-based deepfake detectors where models rely too heavily on high-level semantic cues instead of forgery-specific traces when faced with new data or unseen generation methods. To address this, we propose Geometric Semantic Decoupling (GSD), a simple, parameter-free module that removes semantic components from learned features via a geometric projection, forcing detectors to focus on subtle artifact cues. This approach not only achieves state-of-the-art generalization across diverse deepfake datasets, but also successfully extends to general-scene synthetic images beyond faces, highlighting its broad applicability. By reducing semantic bias, GSD advances the reliability of AI-generated content detection, helping society more effectively identify

deepfakes and other synthetic media, and mitigating the growing risks posed by generative AI.

## Impact Statement

This work focuses on detecting digital forgeries to mitigate the spread of misinformation. All facial images utilized in our experiments are sourced from publicly available datasets (FaceForensics++, Celeb-DF, etc.) and are used in strict accordance with their licenses to respect personal privacy.

## References

- Ba, Z., Liu, Q., Liu, Z., Wu, S., Lin, F., Lu, L., and Ren, K. Exposing the deception: Uncovering more forgery clues for deepfake detection. In *Proceedings of the AAAI Conference on Artificial Intelligence*, volume 38, pp. 719–728, 2024.
- Brock, A., Donahue, J., and Simonyan, K. Large scale gan training for high fidelity natural image synthesis. *arXiv preprint arXiv:1809.11096*, 2018.
- Brown, A. Algorithmic harms: The societal impact of non-consensual ai-generated content. *Nature Machine Intelligence (Perspective)*, 6:112–115, 2024.
- Business, C. Deepfake video conference call swindles multinational firm out of \$25 million, 2024. URL [Anonymouslink].
- Cai, Y., Li, J., Li, Z., Chen, W., Lan, R., Xie, X., Luo, X., and Li, G. Deepshield: Fortifying deepfake video detection with local and global forgery analysis. In *Proceedings of the IEEE/CVF International Conference on Computer Vision*, pp. 12524–12534, 2025.
- Cao, J., Ma, C., Yao, T., Chen, S., Ding, S., and Yang, X. End-to-end reconstruction-classification learning for face forgery detection. In *Proceedings of the IEEE/CVF conference on computer vision and pattern recognition*, pp. 4113–4122, 2022.
- Chai, L., Bau, D., Lim, S.-N., and Isola, P. What makes fake images detectable? understanding properties that generalize. In *European conference on computer vision*, pp. 103–120. Springer, 2020.
- Chen, B., Zeng, J., Yang, J., and Yang, R. Drct: Diffusion reconstruction contrastive training towards universal detection of diffusion generated images. In *Forty-first International Conference on Machine Learning*, 2024.
- Chen, C., Chen, Q., Xu, J., and Koltun, V. Learning to see in the dark. In *Proceedings of the IEEE conference on computer vision and pattern recognition*, pp. 3291–3300, 2018.
- Chen, L., Zhang, Y., Song, Y., Liu, L., and Wang, J. Self-supervised learning of adversarial example: Towards good generalizations for deepfake detection. In *Proceedings of the IEEE/CVF conference on computer vision and pattern recognition*, pp. 18710–18719, 2022.
- Chen, Q. and Koltun, V. Photographic image synthesis with cascaded refinement networks. In *Proceedings of the IEEE international conference on computer vision*, pp. 1511–1520, 2017.
- Chen, Y., Yan, Z., Cheng, G., Zhao, K., Lyu, S., and Wu, B. X2-dfd: A framework for explainable and extendable deepfake detection. In *The Thirty-ninth Annual Conference on Neural Information Processing Systems*.
- Cheng, H., Liu, M.-H., Guo, Y., Wang, T., Nie, L., and Kankanhalli, M. Fair deepfake detectors can generalize. *arXiv preprint arXiv:2507.02645*, 2025a.
- Cheng, J., Yan, Z., Zhang, Y., Luo, Y., Wang, Z., and Li, C. Can we leave deepfake data behind in training deepfake detector? *Advances in Neural Information Processing Systems*, 37:21979–21998, 2024.
- Cheng, S., Lyu, L., Wang, Z., Zhang, X., and Sehwag, V. Co-spy: Combining semantic and pixel features to detect synthetic images by ai. In *Proceedings of the Computer Vision and Pattern Recognition Conference*, pp. 13455–13465, 2025b.
- Choi, Y., Choi, M., Kim, M., Ha, J.-W., Kim, S., and Choo, J. Stargan: Unified generative adversarial networks for multi-domain image-to-image translation. In *Proceedings of the IEEE conference on computer vision and pattern recognition*, pp. 8789–8797, 2018.
- Cozzolino, D., Rössler, A., Thies, J., Nießner, M., and Verdoliva, L. Id-reveal: Identity-aware deepfake video detection. In *Proceedings of the IEEE/CVF international conference on computer vision*, pp. 15108–15117, 2021.
- Cui, X., Li, Y., Luo, A., Zhou, J., and Dong, J. Forensics adapter: Adapting clip for generalizable face forgery detection. In *Proceedings of the Computer Vision and Pattern Recognition Conference*, pp. 19207–19217, 2025.
- Dai, T., Cai, J., Zhang, Y., Xia, S.-T., and Zhang, L. Second-order attention network for single image super-resolution. In *Proceedings of the IEEE/CVF conference on computer vision and pattern recognition*, pp. 11065–11074, 2019.
- Dang, H., Liu, F., Stehouwer, J., Liu, X., and Jain, A. K. On the detection of digital face manipulation. In *Proceedings of the IEEE/CVF Conference on Computer Vision and Pattern recognition*, pp. 5781–5790, 2020.

- Dass, J. and Mahapatra, R. Householder sketch for accurate and accelerated least-mean-squares solvers. In *International Conference on Machine Learning*, pp. 2467–2477. PMLR, 2021.
- Dhariwal, P. and Nichol, A. Diffusion models beat gans on image synthesis. *Advances in neural information processing systems*, 34:8780–8794, 2021a.
- Dhariwal, P. and Nichol, A. Diffusion models beat gans on image synthesis. *Advances in neural information processing systems*, 34:8780–8794, 2021b.
- Dolhansky, B., Howes, R., Pflaum, B., Baram, N., and Ferrer, C. C. The deepfake detection challenge (dfdc) preview dataset. *arXiv preprint arXiv:1910.08854*, 2019.
- Dolhansky, B., Bitton, J., Pflaum, B., Lu, J., Howes, R., Wang, M., and Ferrer, C. C. The deepfake detection challenge (dfdc) dataset. *arXiv preprint arXiv:2006.07397*, 2020.
- Dong, S., Wang, J., Ji, R., Liang, J., Fan, H., and Ge, Z. Implicit identity leakage: The stumbling block to improving deepfake detection generalization. In *Proceedings of the IEEE/CVF conference on computer vision and pattern recognition*, pp. 3994–4004, 2023.
- Dong, X., Bao, J., Chen, D., Zhang, T., Zhang, W., Yu, N., Chen, D., Wen, F., and Guo, B. Protecting celebrities from deepfake with identity consistency transformer. In *Proceedings of the IEEE/CVF conference on computer vision and pattern recognition*, pp. 9468–9478, 2022.
- Frank, J., Eisenhofer, T., Schönherr, L., Fischer, A., Kolossa, D., and Holz, T. Leveraging frequency analysis for deep fake image recognition. In *International conference on machine learning*, pp. 3247–3258. PMLR, 2020.
- Fu, X., Yan, Z., Yao, T., Chen, S., and Li, X. Exploring unbiased deepfake detection via token-level shuffling and mixing. In *Proceedings of the AAAI Conference on Artificial Intelligence*, volume 39, pp. 3040–3048, 2025.
- Gander, W. Algorithms for the qr decomposition. *Res. Rep.*, 80(02):1251–1268, 1980.
- Geirhos, R., Jacobsen, J.-H., Michaelis, C., Zemel, R., Brendel, W., Bethge, M., and Wichmann, F. A. Shortcut learning in deep neural networks. *Nature Machine Intelligence*, 2(11):665–673, 2020.
- Google AI. Contributing data to deepfake detection. [[Anonymous link](#)], 2020. Accessed: 2021-04-24.
- Gu, S., Chen, D., Bao, J., Wen, F., Zhang, B., Chen, D., Yuan, L., and Guo, B. Vector quantized diffusion model for text-to-image synthesis. In *Proceedings of the IEEE/CVF conference on computer vision and pattern recognition*, pp. 10696–10706, 2022.
- Haliassos, A., Vougioukas, K., Petridis, S., and Pantic, M. Lips don’t lie: A generalisable and robust approach to face forgery detection. In *Proceedings of the IEEE/CVF conference on computer vision and pattern recognition*, pp. 5039–5049, 2021.
- Han, Y.-H., Huang, T.-M., Hua, K.-L., and Chen, J.-C. Towards more general video-based deepfake detection through facial component guided adaptation for foundation model. In *Proceedings of the Computer Vision and Pattern Recognition Conference*, pp. 22995–23005, 2025.
- He, K., Zhang, X., Ren, S., and Sun, J. Deep residual learning for image recognition. In *Proceedings of the IEEE conference on computer vision and pattern recognition*, pp. 770–778, 2016.
- Hu, E. J., Shen, Y., Wallis, P., Allen-Zhu, Z., Li, Y., Wang, S., Wang, L., Chen, W., et al. Lora: Low-rank adaptation of large language models. *ICLR*, 1(2):3, 2022.
- Huang, B., Wang, Z., Yang, J., Ai, J., Zou, Q., Wang, Q., and Ye, D. Implicit identity driven deepfake face swapping detection. In *Proceedings of the IEEE/CVF conference on computer vision and pattern recognition*, pp. 4490–4499, 2023.
- Jiang, L., Li, R., Wu, W., Qian, C., and Loy, C. C. Deepforensics-1.0: A large-scale dataset for real-world face forgery detection. In *Proceedings of the IEEE/CVF conference on computer vision and pattern recognition*, pp. 2889–2898, 2020.
- Karras, T., Aila, T., Laine, S., and Lehtinen, J. Progressive growing of gans for improved quality, stability, and variation. *arXiv preprint arXiv:1710.10196*, 2017.
- Karras, T., Laine, S., and Aila, T. A style-based generator architecture for generative adversarial networks. In *Proceedings of the IEEE/CVF conference on computer vision and pattern recognition*, pp. 4401–4410, 2019.
- Kashiani, H., Talemi, N. A., and Afghah, F. Freqdebias: Towards generalizable deepfake detection via consistency-driven frequency debiasing. In *2025 IEEE/CVF Conference on Computer Vision and Pattern Recognition (CVPR)*, pp. 8775–8785. IEEE, 2025.
- Lai, Y., Wang, H., Yang, J., Kang, X., Li, B., Shen, L., and Yu, Z. Gm-df: Generalized multi-scenario deepfake detection. In *Proceedings of the 33rd ACM International Conference on Multimedia*, pp. 4300–4309, 2025.
- Li, J., Xie, H., Li, J., Wang, Z., and Zhang, Y. Frequency-aware discriminative feature learning supervised by

- single-center loss for face forgery detection. In *Proceedings of the IEEE/CVF conference on computer vision and pattern recognition*, pp. 6458–6467, 2021.
- Li, K., Zhang, T., and Malik, J. Diverse image synthesis from semantic layouts via conditional imle. In *Proceedings of the IEEE/CVF International Conference on Computer Vision*, pp. 4220–4229, 2019.
- Li, L., Bao, J., Zhang, T., Yang, H., Chen, D., Wen, F., and Guo, B. Face x-ray for more general face forgery detection. In *Proceedings of the IEEE/CVF conference on computer vision and pattern recognition*, pp. 5001–5010, 2020a.
- Li, Y. and Lyu, S. Exposing deepfake videos by detecting face warping artifacts. In *IEEE Conference on Computer Vision and Pattern Recognition Workshops (CVPRW)*, pp. 2–5, 14, 2019.
- Li, Y., Yang, X., Sun, P., Qi, H., and Lyu, S. Celeb-df: A large-scale challenging dataset for deepfake forensics. In *Proceedings of the IEEE/CVF conference on computer vision and pattern recognition*, pp. 3207–3216, 2020b.
- Li, Z., Li, J., Cai, Y., Chen, J., Luo, X., Li, G., and Lan, R. Fakeradar: Probing forgery outliers to detect unknown deepfake videos. In *Proceedings of the IEEE/CVF International Conference on Computer Vision*, pp. 13382–13392, 2025.
- Lin, Y., Song, W., Li, B., Li, Y., Ni, J., Chen, H., and Li, Q. Fake it till you make it: Curricular dynamic forgery augmentations towards general deepfake detection. In *European conference on computer vision*, pp. 104–122. Springer, 2024.
- Liu, H., Li, X., Zhou, W., Chen, Y., He, Y., Xue, H., Zhang, W., and Yu, N. Spatial-phase shallow learning: rethinking face forgery detection in frequency domain. In *Proceedings of the IEEE/CVF conference on computer vision and pattern recognition*, pp. 772–781, 2021a.
- Liu, H., Tan, Z., Tan, C., Wei, Y., Wang, J., and Zhao, Y. Forgery-aware adaptive transformer for generalizable synthetic image detection. In *Proceedings of the IEEE/CVF Conference on Computer Vision and Pattern Recognition*, pp. 10770–10780, 2024a.
- Liu, Z., Qi, X., and Torr, P. H. Global texture enhancement for fake face detection in the wild. In *Proceedings of the IEEE/CVF conference on computer vision and pattern recognition*, pp. 8060–8069, 2020.
- Liu, Z., Lin, Y., Cao, Y., Hu, H., Wei, Y., Zhang, Z., Lin, S., and Guo, B. Swin transformer: Hierarchical vision transformer using shifted windows. In *Proceedings of the IEEE/CVF international conference on computer vision*, pp. 10012–10022, 2021b.
- Liu, Z., Wang, H., Kang, Y., and Wang, S. Mixture of low-rank experts for transferable ai-generated image detection. *arXiv preprint arXiv:2404.04883*, 2024b.
- Loshchilov, I. and Hutter, F. Decoupled weight decay regularization. *arXiv preprint arXiv:1711.05101*, 2017.
- Luo, A., Kong, C., Huang, J., Hu, Y., Kang, X., and Kot, A. C. Beyond the prior forgery knowledge: Mining critical clues for general face forgery detection. *IEEE Transactions on Information Forensics and Security*, 19:1168–1182, 2023.
- Ma, L., Yan, Z., Xu, J., Chen, Y., Guo, Q., Bi, Z., Liao, Y., and Lin, H. From specificity to generality: Revisiting generalizable artifacts in detecting face deepfakes. *arXiv preprint arXiv:2504.04827*, 2025.
- Maaten, L. v. d. and Hinton, G. Visualizing data using t-sne. *Journal of machine learning research*, 9(Nov): 2579–2605, 2008.
- Masi, I., Killekar, A., Mascarenhas, R. M., Gurudatt, S. P., and AbdAlmageed, W. Two-branch recurrent network for isolating deepfakes in videos. In *European conference on computer vision*, pp. 667–684. Springer, 2020.
- Midjourney. Midjourney. [[Anonymouslink](#)], 2022. Accessed: 2026-01-04.
- Nataraj, L., Mohammed, T. M., Chandrasekaran, S., Flenner, A., Bappy, J. H., Roy-Chowdhury, A. K., and Manjunath, B. Detecting gan generated fake images using co-occurrence matrices. *arXiv preprint arXiv:1903.06836*, 2019.
- Ni, Y., Meng, D., Yu, C., Quan, C., Ren, D., and Zhao, Y. Core: Consistent representation learning for face forgery detection. In *Proceedings of the IEEE/CVF conference on computer vision and pattern recognition*, pp. 12–21, 2022.
- Nichol, A., Dhariwal, P., Ramesh, A., Shyam, P., Mishkin, P., McGrew, B., Sutskever, I., and Chen, M. Glide: Towards photorealistic image generation and editing with text-guided diffusion models. *arXiv preprint arXiv:2112.10741*, 2021.
- Niu, Y., Chen, Y., and Zhang, L. Detecting ai-generated images via distributional deviations from real images. *arXiv preprint arXiv:2601.03586*, 2026.
- Ojha, U., Li, Y., and Lee, Y. J. Towards universal fake image detectors that generalize across generative models. In *Proceedings of the IEEE/CVF Conference on Computer Vision and Pattern Recognition*, pp. 24480–24489, 2023.

- Park, T., Liu, M.-Y., Wang, T.-C., and Zhu, J.-Y. Semantic image synthesis with spatially-adaptive normalization. In *Proceedings of the IEEE/CVF conference on computer vision and pattern recognition*, pp. 2337–2346, 2019.
- Qian, Y., Yin, G., Sheng, L., Chen, Z., and Shao, J. Thinking in frequency: Face forgery detection by mining frequency-aware clues. In *European conference on computer vision*, pp. 86–103. Springer, 2020.
- Radford, A., Kim, J. W., Hallacy, C., Ramesh, A., Goh, G., Agarwal, S., Sastry, G., Askell, A., Mishkin, P., Clark, J., et al. Learning transferable visual models from natural language supervision. In *International conference on machine learning*, pp. 8748–8763. Pmlr, 2021.
- Ramesh, A., Pavlov, M., Goh, G., Gray, S., Voss, C., Radford, A., Chen, M., and Sutskever, I. Zero-shot text-to-image generation. In *International conference on machine learning*, pp. 8821–8831. Pmlr, 2021.
- Rombach, R., Blattmann, A., Lorenz, D., Esser, P., and Ommer, B. High-resolution image synthesis with latent diffusion models. In *Proceedings of the IEEE/CVF conference on computer vision and pattern recognition*, pp. 10684–10695, 2022.
- Rossler, A., Cozzolino, D., Verdoliva, L., Riess, C., Thies, J., and Nießner, M. Faceforensics++: Learning to detect manipulated facial images. In *Proceedings of the IEEE/CVF international conference on computer vision*, pp. 1–11, 2019.
- Shiohara, K. and Yamasaki, T. Detecting deepfakes with self-blended images. In *Proceedings of the IEEE/CVF conference on computer vision and pattern recognition*, pp. 18720–18729, 2022.
- Shuai, C., Zhong, J., Wu, S., Lin, F., Wang, Z., Ba, Z., Liu, Z., Cavallaro, L., and Ren, K. Locate and verify: A two-stream network for improved deepfake detection. In *Proceedings of the 31st ACM International Conference on Multimedia*, pp. 7131–7142, 2023.
- Sun, K., Yao, T., Chen, S., Ding, S., Li, J., and Ji, R. Dual contrastive learning for general face forgery detection. In *Proceedings of the AAAI conference on artificial intelligence*, volume 36, pp. 2316–2324, 2022.
- Sun, K., Chen, S., Yao, T., Liu, H., Sun, X., Ding, S., and Ji, R. Diffusionfake: Enhancing generalization in deepfake detection via guided stable diffusion. *Advances in Neural Information Processing Systems*, 37:101474–101497, 2024.
- Tan, C., Zhao, Y., Wei, S., Gu, G., and Wei, Y. Learning on gradients: Generalized artifacts representation for gan-generated images detection. In *Proceedings of the IEEE/CVF Conference on Computer Vision and Pattern Recognition*, pp. 12105–12114, 2023.
- Tan, C., Zhao, Y., Wei, S., Gu, G., Liu, P., and Wei, Y. Frequency-aware deepfake detection: Improving generalizability through frequency space domain learning. In *Proceedings of the AAAI Conference on Artificial Intelligence*, volume 38, pp. 5052–5060, 2024a.
- Tan, C., Zhao, Y., Wei, S., Gu, G., Liu, P., and Wei, Y. Rethinking the up-sampling operations in cnn-based generative network for generalizable deepfake detection. In *Proceedings of the IEEE/CVF Conference on Computer Vision and Pattern Recognition*, pp. 28130–28139, 2024b.
- Tan, C., Tao, R., Liu, H., Gu, G., Wu, B., Zhao, Y., and Wei, Y. C2p-clip: Injecting category common prompt in clip to enhance generalization in deepfake detection. In *Proceedings of the AAAI Conference on Artificial Intelligence*, volume 39, pp. 7184–7192, 2025.
- Tan, M. and Le, Q. Efficientnet: Rethinking model scaling for convolutional neural networks. In *International conference on machine learning*, pp. 6105–6114. PMLR, 2019.
- Touvron, H., Cord, M., Douze, M., Massa, F., Sablayrolles, A., and Jégou, H. Training data-efficient image transformers & distillation through attention. In *International conference on machine learning*, pp. 10347–10357. PMLR, 2021.
- Wang, S.-Y., Wang, O., Zhang, R., Owens, A., and Efros, A. A. Cnn-generated images are surprisingly easy to spot... for now. In *Proceedings of the IEEE/CVF conference on computer vision and pattern recognition*, pp. 8695–8704, 2020.
- Wang, Z., Cheng, Z., Xiong, J., Xu, X., Li, T., Veeravalli, B., and Yang, X. A timely survey on vision transformer for deepfake detection. *arXiv preprint arXiv:2405.08463*, 2024.
- Wukong. Wukong. <https://xihe.mindspore.cn/modelzoo/wukong>, May 2022. Accessed: 2026-01-04.
- Xie, S., Qiao, T., Li, S., Zhang, X., Zhou, J., and Feng, G. Deepfake detection in the aigc era: A survey, benchmarks, and future perspectives. *Information Fusion*, pp. 103740, 2025.
- Xu, Z., Zhang, X., Li, R., Tang, Z., Huang, Q., and Zhang, J. Fakeshield: Explainable image forgery detection and localization via multi-modal large language models. *arXiv preprint arXiv:2410.02761*, 2024.

- Yan, Z., Zhang, Y., Fan, Y., and Wu, B. Ucf: Uncovering common features for generalizable deepfake detection. In *Proceedings of the IEEE/CVF international conference on computer vision*, pp. 22412–22423, 2023a.
- Yan, Z., Zhang, Y., Yuan, X., Lyu, S., and Wu, B. Deepfakebench: A comprehensive benchmark of deepfake detection. *arXiv preprint arXiv:2307.01426*, 2023b.
- Yan, Z., Luo, Y., Lyu, S., Liu, Q., and Wu, B. Transcending forgery specificity with latent space augmentation for generalizable deepfake detection. In *Proceedings of the IEEE/CVF Conference on Computer Vision and Pattern Recognition*, pp. 8984–8994, 2024a.
- Yan, Z., Wang, J., Wang, Z., Jin, P., Zhang, K.-Y., Chen, S., Yao, T., Ding, S., Wu, B., and Yuan, L. Effort: Efficient orthogonal modeling for generalizable ai-generated image detection. *arXiv preprint arXiv:2411.15633*, 2, 2024b.
- Yan, Z., Yao, T., Chen, S., Zhao, Y., Fu, X., Zhu, J., Luo, D., Wang, C., Ding, S., Wu, Y., et al. Df40: Toward next-generation deepfake detection. *Advances in Neural Information Processing Systems*, 37:29387–29434, 2024c.
- Yan, Z., Zhao, Y., Chen, S., Guo, M., Fu, X., Yao, T., Ding, S., Wu, Y., and Yuan, L. Generalizing deepfake video detection with plug-and-play: Video-level blending and spatiotemporal adapter tuning. In *Proceedings of the Computer Vision and Pattern Recognition Conference*, pp. 12615–12625, 2025.
- Zhang, X., Karaman, S., and Chang, S.-F. Detecting and simulating artifacts in gan fake images. In *2019 IEEE international workshop on information forensics and security (WIFS)*, pp. 1–6. IEEE, 2019.
- Zhao, C., Wang, K., Zeng, X., Zhao, R., and Chan, A. B. Gradient-based visual explanation for transformer-based clip. In *International Conference on Machine Learning*, pp. 61072–61091. PMLR, 2024.
- Zhao, H., Zhou, W., Chen, D., Wei, T., Zhang, W., and Yu, N. Multi-attentional deepfake detection. In *Proceedings of the IEEE/CVF conference on computer vision and pattern recognition*, pp. 2185–2194, 2021.
- Zhu, J.-Y., Park, T., Isola, P., and Efros, A. A. Unpaired image-to-image translation using cycle-consistent adversarial networks. In *Proceedings of the IEEE international conference on computer vision*, pp. 2223–2232, 2017.
- Zhu, M., Chen, H., Yan, Q., Huang, X., Lin, G., Li, W., Tu, Z., Hu, H., Hu, J., and Wang, Y. Genimage: A million-scale benchmark for detecting ai-generated image. *Advances in Neural Information Processing Systems*, 36: 77771–77782, 2023.

# Supplementary Materials for

## *Geometric Semantic Decoupling for Generalizable AI-Generated Image Detection*

### A. Implementation Details

#### A.1. Datasets and Evaluation Details

We consider two evaluation regimes: **face forgery detection** and **synthetic image detection**. Each regime follows its standard training protocol, as detailed below.

**Face Forgery Detection.** We use FaceForensics++ (FF++) (Rossler et al., 2019) as the source domain and adopt the High-Quality (c23) compression setting, consistent with DeepfakeBench (Yan et al., 2023b). **(i) Cross-dataset generalization:** Models trained on FF++ are evaluated on unseen target datasets, including Celeb-DF-v1/v2 (Li et al., 2020b), DFD (Google AI, 2020), DFDC (Dolhansky et al., 2020), and DFDCP (Dolhansky et al., 2019). **(ii) Cross-manipulation generalization:** We evaluate generalization to novel manipulation techniques using a subset of DF40 (Yan et al., 2024c), where we use a six-type representative forgery subset.

**Synthetic Image Detection.** To assess detection performance on synthetic imagery, we additionally benchmark on UniversalFakeDetect (Ojha et al., 2023) and GenImage (Zhu et al., 2023). **(i) UniversalFakeDetect:** UniversalFakeDetect (Ojha et al., 2023) includes both GAN-based and diffusion-based generators. The GAN-based subset covers, *e.g.*, CycleGAN (Zhu et al., 2017), BigGAN (Brock et al., 2018), StyleGAN (Karras et al., 2019), GauGAN (Park et al., 2019), and StarGAN (Choi et al., 2018), as well as several content-aware synthesis pipelines (*e.g.*, DeepFakes (Rossler et al., 2019), SITD (Chen et al., 2018), SAN (Dai et al., 2019), CRN (Chen & Koltun, 2017), and IMLE (Li et al., 2019)). The diffusion-based subset includes, *e.g.*, Guided Diffusion (Dhariwal & Nichol, 2021b), LDM/Stable Diffusion (Rombach et al., 2022), GLIDE (Nichol et al., 2021), and DALL-E (Ramesh et al., 2021). Following the protocol in (Ojha et al., 2023), we train on the ProGAN dataset and evaluate on the remaining unseen 19 test sets covering diverse generative sources. **(ii) GenImage:** GenImage (Zhu et al., 2023) consists primarily of high-quality diffusion images, including Midjourney (Midjourney, 2022), Stable Diffusion v1.4/v1.5 (Rombach et al., 2022), ADM (Dhariwal & Nichol, 2021a), GLIDE (Nichol et al., 2021), Wukong (Wukong, 2022), VQDM (Gu et al., 2022), and BigGAN (Brock et al., 2018). Following the standard cross-model protocol in GenImage (Zhu et al., 2023), SD v1.4 is used for training and the remaining generators are used for testing.

#### A.2. Baseline Detectors

This subsection lists the full set of baseline detectors used in our benchmark, grouped into **(i) foundation/backbone baselines**, **(ii) face-forgery detectors**, and **(iii) synthetic-image (AIGC) detectors**. For each method, we report the evaluation results either by running the **officially released checkpoints** or by using an **official reproduction**. When neither is available, we cite results from prior work for fair comparison.

**(i) Foundation baselines.** We include commonly used architectures and foundation models as generic feature extractors or end-to-end classifiers: Efficient-b4 (Tan & Le, 2019), ResNet-50 (He et al., 2016), DeiT-S (Touvron et al., 2021), Swin-T (Liu et al., 2021b), and CLIP (Radford et al., 2021).

**(ii) Face-forgery detectors.** We benchmark against representative face forgery/deepfake detectors, including F3Net (Qian et al., 2020), Face X-Ray (Li et al., 2020a), RECCE (Cao et al., 2022), SBIs (Shiohara & Yamasaki, 2022), LSDA (Yan et al., 2024a), FCG (Han et al., 2025), ProDet (Cheng et al., 2024), VbSaT (Yan et al., 2025), DeepShield (Cai et al., 2025),  $\chi^2$ -DFD (Chen et al.), CDFA (Lin et al., 2024), Effort (Yan et al., 2024b), FreqDebias (Kashiani et al., 2025), LaV (Shuai et al., 2023), CFM (Luo et al., 2023), IID (Huang et al., 2023), UCF (Yan et al., 2023a), FakeRadar (Li et al., 2025), ExposDe (Ba et al., 2024), FSgD (Ma et al., 2025), RAID (Cheng et al., 2025a), UDD (Fu et al., 2025), DFFake (Sun et al., 2024), ICT (Dong et al., 2022), ForAda (Cui et al., 2025), and GM-DF (Lai et al., 2025).

**(iii) Synthetic-image (AIGC) detectors.** We also compare with detectors designed for AI-generated imagery and general image forensics, including CNN-Spot (Wang et al., 2020), PatchForensics (Chai et al., 2020), Co-occurrence (Nataraj et al., 2019), Freq-spec (Zhang et al., 2019), GramNet (Liu et al., 2020), UniFD (Ojha et al., 2023), LGrad (Tan et al.,

2023), NPR (Tan et al., 2024b), FreqNet (Tan et al., 2024a), FatFormer (Liu et al., 2024a), CLIPMoLe (Liu et al., 2024b), DRCT (Chen et al., 2024), C2P (Tan et al., 2025), and MPFT (Niu et al., 2026).

## B. Limitations and Future Work

While our Geometric Semantic Decoupling (GSD) module effectively suppresses dominant semantic components via orthogonal projection, the resulting learning in the semantic null space is still largely representation-driven rather than explicitly cue-aligned. In particular, we do not impose fine-grained constraints on the residual features after decoupling; consequently, these non-semantic residuals are not guaranteed to correspond to concrete physical manipulation traces (*e.g.*, blending boundaries or frequency artifacts). In future work, we will explore data construction and supervision strategies that encourage the decoupled residuals to align with specific forgery cues, for example by synthesizing cue-targeted perturbations or injecting localized trace priors into the null-space learning process.

## C. More Related Work

**Generalizable Deepfake Detection.** Deepfake detection has evolved from discerning specific manipulation signatures to seeking generalized forensic traces. Early approaches predominantly focused on mining low-level artifacts, such as frequency spectrum anomalies (Qian et al., 2020; Kashiani et al., 2025; Li et al., 2021), blending boundaries (Li et al., 2020a; Chen et al., 2022; Tan et al., 2023), and local textural inconsistencies (Liu et al., 2021a; Masi et al., 2020; Frank et al., 2020). To capture subtle cues beyond global statistics, fine-grained spatio-temporal modeling (Dang et al., 2020; Zhao et al., 2021; Haliassos et al., 2021) and consistency checking (Dong et al., 2022; Cozzolino et al., 2021; Sun et al., 2022) were introduced to verify identity or biological coherence. Despite these advances, supervised detectors often overfit to dataset-specific patterns. To mitigate this, a prominent line of work employs data synthesis to simulate a wider range of forgery distributions. For instance, SBI (Shiohara & Yamasaki, 2022) and similar methods (Cheng et al., 2024; Ma et al., 2025) synthesize “pseudo-fakes” using blending augmentations, encouraging models to learn generic blending boundaries rather than method-specific artifacts.

Driven by the remarkable generalization capabilities of large-scale pre-training, recent research has pivoted toward leveraging Vision Foundation Models (VFM)s, such as CLIP (Radford et al., 2021), as primary backbones. Unlike traditional detectors trained from scratch, VFMs offer robust, open-world feature representations derived from vast web-scale data. Prominent approaches, including Forensics Adapter (Cui et al., 2025) injects lightweight adapter modules to align generic features with forgery cues. Yan et al. (2024b) involves the SVD to construct explicit orthogonality for preserving pre-trained knowledge and learning forgery-related patterns, avoiding the distortion of well-learned pre-trained knowledge during learning forgeries. In the video domain, frameworks such as FCG (Han et al., 2025), VbSaT (Yan et al., 2025), and DeepShield (Cai et al., 2025) extend frozen image backbones with plug-and-play spatiotemporal modules to capture temporal inconsistencies. Furthermore, the emergent wave of Multimodal Large Language Models (MLLMs) integrates these visual encoders with LLMs to facilitate interpretable, reasoning-driven detection (Chen et al.; Xu et al., 2024). However, a critical side effect of this paradigm is that VFMs are inherently optimized for semantic alignment (*e.g.*, matching images to object texts). This creates a fundamental conflict: the backbone’s strong bias toward high-level semantics (*e.g.*, identity) can overshadow the subtle, low-level artifacts required for effective forgery detection, necessitating explicit mechanisms to suppress this semantic dominance.

**Generalizable Synthetic Image Detection.** The evolution of synthetic image detection has progressed from mining low-level artifacts to harnessing the power of Vision Foundation Models (VFMs). Initially, researchers focused on identifying intrinsic generator fingerprints to differentiate real from fake. For instance, CNNSpot (Wang et al., 2020) targets specific texture and spectral patterns to isolate generator-specific signatures, while Patchfor (Chai et al., 2020) adopts a patch-based strategy, strictly constraining the receptive field to force the network to scrutinize local forensic anomalies rather than semantic content. LGrad (Tan et al., 2023) takes a unique angle by transforming images into gradient maps, leveraging pre-trained generative priors to expose generalized manipulation traces that persist across different GAN architectures.

With the advent of large-scale pre-training, the focus shifted toward adapting VFMs like CLIP. UnivFD (Ojha et al., 2023) established a strong baseline by utilizing frozen CLIP features directly with lightweight classifiers, validating the inherent forensic utility of open-world representations. To further align these generic features with forensic tasks without heavy retraining, recent studies have embraced parameter-efficient tuning. FatFormer (Liu et al., 2024a) introduces distinct adapter modules to recalibrate intermediate representations, whereas C2P-CLIP (Tan et al., 2025) enhances adaptation by

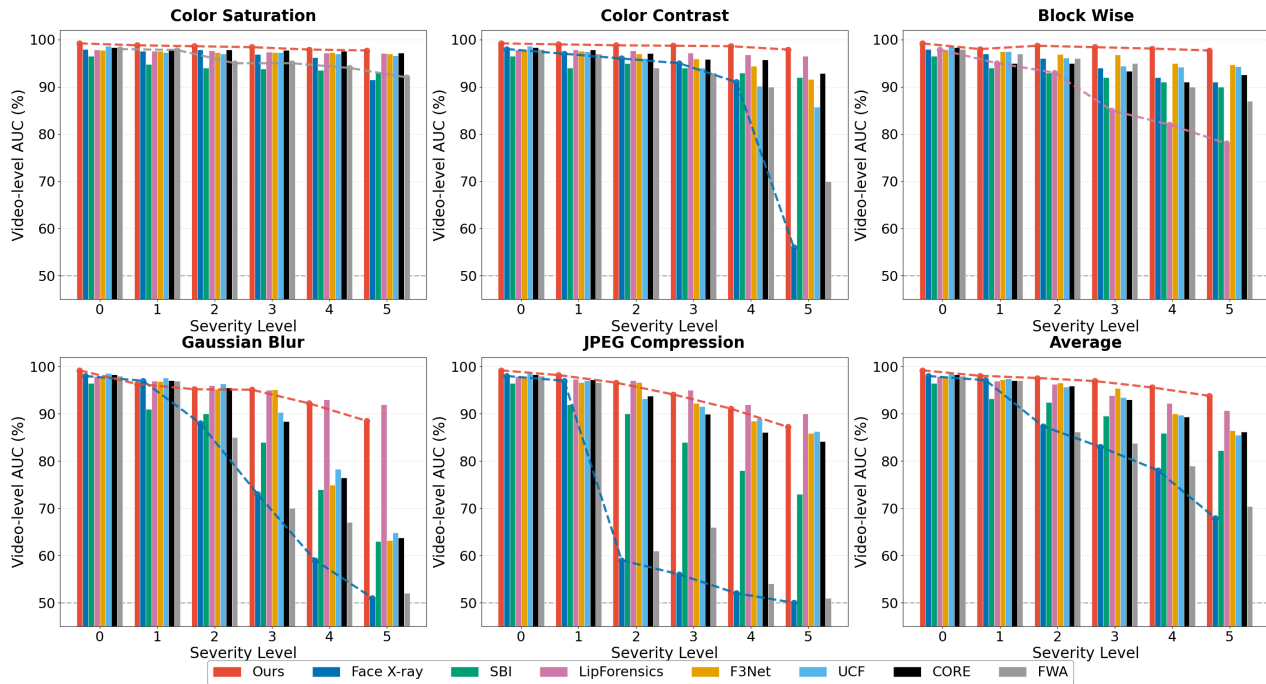


Figure 7. Robustness analysis against common image corruptions. The curves illustrate the Video-level AUC (%) performance of our method versus existing approaches. We test across five different degradation scenarios, including Color Saturation, JPEG Compression, Color Contrast, Block-wise noise, and Gaussian Blur, plotted against increasing severity levels (0-5).

injecting category-aware prompts and applying Low-Rank Adaptation (LoRA) specifically to the attention mechanisms. Similarly, CLIPMoLE (Liu et al., 2024b) employs a Mixture-of-Experts (MoE) strategy, inserting low-rank experts into deeper layers to dynamic adjust feature abstraction for better transferability. Beyond pure adaptation, hybrid frameworks like CO-SPY (Cheng et al., 2025b) explore feature synergism, fusing semantic CLIP embeddings with reconstruction-guided residuals to combine high-level consistency with low-level artifact detection.

## D. Additional Results

### D.1. Robustness Evaluation

To assess the resilience of our model against real-world image distortions, we follow the rigorous evaluation protocols established in prior studies (Haliassos et al., 2021; Yan et al., 2024b;a; Jiang et al., 2020). The assessment covers five distinct degradation categories: Color Saturation, JPEG Compression, Color Contrast, Block-wise artifacts, and Gaussian Blur. For each category, we apply distortions ranging from severity level 0 to 5 to measure performance stability. All models are trained on the FaceForensics++ (c23) dataset and evaluated using video-level AUC. We benchmark our approach against leading methods such as Face X-ray (Li et al., 2020a), SBI (Shiohara & Yamasaki, 2022), LipForensics (Haliassos et al., 2021), and FWA (Li & Lyu, 2019). To ensure a controlled comparison, we also reproduced F3Net (Qian et al., 2020), UCF (Yan et al., 2023a), and CORE (Ni et al., 2022) using **the same data augmentation pipeline** employed in our framework.

The quantitative results are presented in Figure 7. As shown in the “Average” plot, our method consistently secures the top performance across nearly all severity levels, outperforming both the standard baselines and the reproduced counterparts sharing identical augmentation schemes. While competitors experience sharp performance declines under severe distortions, specifically in JPEG compression and Gaussian blur where high-frequency details are compromised, our model exhibits superior stability. This evidence confirms that the robustness of our method is intrinsic to the learned generalized features rather than being a byproduct of data augmentation.

## D.2. GenImage Benchmark

To specifically assess performance on state-of-the-art diffusion generators, we additionally use the GenImage dataset (Zhu et al., 2023). Following the standard cross-model protocol in GenImage (Zhu et al., 2023), we train the detector on **SD v1.4** and evaluate it on the remaining generators to measure **cross-generator generalization**. Table 6 reports the ACC(%) results. Overall, our method achieves the **best average accuracy of 92.8%**, outperforming strong recent detectors such as Effort (Yan et al., 2024b) (91.1%), DRCT (Chen et al., 2024) (89.5%), and FatFormer (Liu et al., 2024a) (88.9%). Notably, despite being trained only on SD v1.4, our model generalizes well to diverse diffusion engines, achieving 88.2% on Midjourney, 84.2% on ADM, 91.6% on GLIDE, and near-saturated performance on several sources (e.g., 99.5% on VQDM and 100.0% on Wukong). We observe comparatively lower accuracy on BigGAN (79.3%), which is expected since it is a GAN-based generator with a different artifact profile; nevertheless, our method remains competitive and yields the strongest overall robustness across generators.

Table 6. Benchmarking results of cross-method evaluations in terms of ACC (%) performance on the Genimage dataset. Following (Zhu et al., 2023), SDv1.4 is used for training, and others are used for testing. Some results of the compared methods are cited from (Yan et al., 2024b). The best results in each column are highlighted in **bold**.

Methods	Midjourney	SDv1.4	SDv1.5	ADM	GLIDE	Wukong	VQDM	BigGAN	Avg.
ResNet-50 (CVPR’16)	54.9	99.9	99.7	53.5	61.9	98.2	56.6	52.0	72.1
DeiT-S (ICML’21)	55.6	99.9	99.8	49.8	58.1	98.9	56.9	53.5	71.6
Swin-T (ICCV’21)	62.1	99.9	99.8	49.8	67.6	99.1	62.3	57.6	74.8
CNNSpot (CVPR’20)	52.8	96.3	95.9	50.1	39.8	78.6	53.4	46.8	64.2
Freq-spec (WIFS’20)	52.0	99.4	99.2	49.7	49.8	94.8	55.6	49.8	68.8
F3Net (ECCV’20)	50.1	99.9	<b>99.9</b>	49.9	50.0	99.9	49.9	49.9	68.7
GramNet (CVPR’20)	54.2	99.2	99.1	50.3	54.6	98.9	50.8	51.7	69.9
UnivFD (CVPR’23)	91.5	96.4	96.1	58.1	73.4	94.5	67.8	57.7	79.5
CLIPMoLE (Arxiv’24)	77.5	86.9	87.2	<b>85.7</b>	<b>94.1</b>	86.6	92.0	<b>99.0</b>	88.6
NPR (CVPR’24)	81.0	98.2	97.9	76.9	89.8	96.9	84.1	84.2	88.6
FreqNet (AAAI’24)	89.6	98.8	98.6	66.8	86.5	97.3	75.8	81.4	86.8
FatFormer (CVPR’24)	<b>92.7</b>	<b>100.0</b>	<b>99.9</b>	75.9	88.0	99.9	98.8	55.8	88.9
DRCT (ICML’24)	91.5	95.0	94.4	79.4	89.2	94.7	90.0	81.7	89.5
Effort (ICML’25)	82.4	99.8	99.8	78.7	93.3	97.4	91.7	77.6	91.1
Ours	88.2	<b>100.0</b>	<b>99.9</b>	84.2	91.6	<b>100.0</b>	<b>99.5</b>	79.3	<b>92.8</b>

## E. Additional Ablation Studies

### E.1. Ablation on the GSD Insertion Depth

Here, we provide a granular performance breakdown across all benchmarks to empirically validate this hyperparameter choice. We conducted a grid search for  $N \in \{2, 4, 8, 12\}$ , and the detailed Accuracy and AUC scores are reported in Table 7, respectively.

Our analysis reveals three distinct regimes of model behavior:

- **Regime of Feature Corruption ( $N = 12$ ):** As hypothesized, applying GSD to shallower layers (Block 12 to 24) is detrimental. The quantitative data supports this: Accuracy on CDF-v2 drops significantly from 83.5% ( $N = 4$ ) to 79.8% ( $N = 12$ ). Similarly, AUC on FaceDancer degrades by 1.6% compared to the optimal setting. This empirical evidence confirms that early intervention interferes with the preservation of low-level forensic signatures (e.g., high-frequency noise), leading to a generalized performance degradation.
- **Regime of Incomplete Decoupling ( $N = 2$ ):** Restricting the module to only the final two layers results in “underfitting” the geometric subspace. While  $N = 2$  outperforms  $N = 12$  on some datasets (e.g., DFD AUC: 94.1% vs. 92.6%), it consistently lags behind  $N = 4$ . For instance, on the challenging FaceDancer dataset,  $N = 2$  achieves an AUC of 92.1%, which is 1.6% lower than the peak performance of 93.7% at  $N = 4$ . This suggests that a depth of 2 blocks is insufficient to fully isolate the semantic components before the classification head.
- **Optimal Stability Regime ( $N = 4$  vs.  $N = 8$ ):** The comparison between  $N = 4$  and  $N = 8$  reveals an interesting trade-off between cross-dataset adaptation and cross-manipulation generalization. Specifically,  $N = 8$  exhibits a slight

Table 7. Ablation studies on insertion depth  $N$  in terms of Accuracy (ACC) and AUC (%).

$N$	Metric	CDF-v2	CDF-v1	DFDC	DFDCP	DFD	InSwap	FSGAN	e4s	SimSwap	UniFace	FaceDancer
$N=2$	ACC	78.8	82.1	<b>77.2</b>	80.6	88.9	82.3	90.2	91.2	81.9	86.6	83.3
	AUC	87.5	89.8	<b>85.7</b>	89.2	94.1	89.9	96.2	97.5	89.8	94.4	92.1
$N=4$	ACC	<b>83.5</b>	82.6	76.3	80.9	91.0	<b>84.5</b>	<b>90.4</b>	<b>92.8</b>	<b>83.6</b>	<b>89.0</b>	<b>87.0</b>
	AUC	<b>90.6</b>	91.0	85.5	<b>89.9</b>	94.3	92.1	96.1	<b>97.9</b>	<b>91.0</b>	<b>96.1</b>	<b>93.7</b>
$N=8$	ACC	82.2	<b>83.6</b>	76.4	<b>81.5</b>	<b>91.2</b>	80.9	<b>90.4</b>	91.4	77.3	84.8	81.9
	AUC	89.7	<b>94.9</b>	85.6	89.7	<b>94.4</b>	91.6	<b>96.4</b>	97.0	88.2	94.7	91.8
$N=12$	ACC	79.8	79.1	74.1	78.0	89.5	80.5	89.4	90.2	78.5	85.8	81.8
	AUC	88.9	88.0	82.9	85.5	92.6	<b>92.6</b>	95.6	96.6	86.8	94.7	92.1

advantage in cross-dataset scenarios, achieving marginally higher Accuracy on benchmarks like CDF-v1 (83.6% vs. 82.6%) and DFD (91.2% vs. 91.0%). This suggests that a deeper insertion allows the model to better adapt to domain shifts (e.g., lighting, compression) present in different datasets. However,  $N = 4$  demonstrates significantly superior robustness against unseen manipulation types (DF40). As shown in Table 7, increasing the depth to  $N = 8$  causes a sharp performance drop on unseen algorithms, such as SimSwap (Acc: 83.6%  $\rightarrow$  77.3%) and FaceDancer (Acc: 87.0%  $\rightarrow$  81.9%).

## E.2. Extended Analysis on Subspace Dimensionality

We present the full-scale experimental results in Table 8 to analyze the impact of semantic subspace configuration  $K$ . As a supplement to Table 4, this table details both Accuracy (ACC) and AUC metrics across the entire suite of 11 evaluation benchmarks, covering diverse domains from cross-datasets (e.g., CDF-v2, DFDC) to cross-manipulation (e.g., SimSwap, FaceDancer).

Table 8. Ablation studies on  $K$  (frame-level AUC and ACC (%)).

$K$	Metric	CDF-v2	CDF-v1	DFDCP	DFD	DFDC	SimSwap	UniFace	e4s	FaceDancer	FSGAN	InSwap
$K=2$	ACC	82.8	82.7	<b>81.2</b>	90.8	<b>77.1</b>	<b>84.0</b>	<b>89.0</b>	<b>93.0</b>	87.1	90.5	<b>84.9</b>
	AUC	90.1	90.4	89.1	94.1	85.8	<b>91.6</b>	95.8	97.9	<b>93.7</b>	96.2	<b>92.1</b>
$K=8$	ACC	82.6	<b>82.9</b>	80.7	90.9	76.7	83.5	<b>89.0</b>	92.6	<b>87.4</b>	90.1	84.7
	AUC	90.3	<b>92.0</b>	89.7	94.1	85.5	90.9	96.0	<b>98.0</b>	<b>93.7</b>	96.2	92.0
$K=16$	ACC	<b>83.5</b>	82.6	80.9	91.0	76.3	83.6	<b>89.0</b>	92.8	87.0	90.4	84.5
	AUC	90.6	91.0	89.9	<b>94.3</b>	85.5	91.0	<b>96.1</b>	97.9	<b>93.7</b>	96.1	<b>92.1</b>
$K=32$	ACC	83.3	82.8	80.2	90.4	76.7	82.9	88.8	92.3	86.8	90.5	84.0
	AUC	90.5	91.9	<b>90.0</b>	<b>94.3</b>	85.6	90.4	96.0	97.7	93.6	96.1	91.8
$K=64$	ACC	82.5	82.7	80.4	<b>91.2</b>	76.8	83.4	88.7	92.4	86.8	<b>90.7</b>	83.8
	AUC	<b>90.7</b>	90.9	89.9	<b>94.3</b>	<b>85.9</b>	90.6	<b>96.1</b>	97.8	93.4	<b>96.3</b>	91.8

## E.3. Ablation on Feature Aggregation for Semantic Consensus

To supplement the analysis in Table 5, we provide the complete quantitative comparison between Global Average Pooling (GAP) and the [CLS] token in Table 9. The extended results corroborate the stability of the GAP strategy; it achieves superior or comparable performance across the vast majority of metrics.

## F. Feature Analysis

### F.1. More t-SNE Visualization

This subsection provides additional embedding-space analyses to complement Observations I–III (Section 1) in the main text. We study two broad regimes: **face forgery** and **natural-image synthesis**. For face forgery, we evaluate generalization under (i) a cross-domain shift on DFDC and (ii) a cross-manipulation shift on FSGAN. Beyond faces, we further analyze

Table 9. The comparison of the global average pooling and the [CLS] token to represent the semantic center.

Method	Metric	CDF-v2	CDF-v1	DFDCP	DFD	DFDC	SimSwap	UniFace	e4s	FaceDancer	FSGAN	InSwap
Avg-Pooling	ACC	<b>83.5</b>	<b>82.6</b>	<b>80.9</b>	<b>91.0</b>	76.3	83.6	89.0	<b>92.8</b>	<b>87.0</b>	<b>90.4</b>	<b>84.5</b>
	AUC	<b>90.6</b>	<b>91.0</b>	<b>89.9</b>	<b>94.3</b>	<b>85.5</b>	91.0	<b>96.1</b>	<b>97.9</b>	<b>93.7</b>	<b>96.1</b>	<b>92.1</b>
	Video-AUC	<b>96.4</b>	<b>96.4</b>	<b>93.2</b>	<b>97.7</b>	<b>88.3</b>	95.6	<b>98.6</b>	<b>99.5</b>	<b>97.5</b>	<b>98.8</b>	96.6
[CLS] Token	ACC	80.2	81.2	80.8	90.3	<b>76.6</b>	<b>83.8</b>	<b>89.1</b>	92.4	86.9	89.7	83.4
	AUC	89.2	88.8	88.7	<b>94.3</b>	<b>85.5</b>	<b>91.9</b>	95.9	97.8	93.6	96.0	91.8
	Video-AUC	94.6	95.3	92.7	97.5	88.1	<b>96.4</b>	98.3	99.4	97.3	98.5	<b>96.8</b>

synthetic images from UniversalFakeDetect, focusing on the ProGAN subset. The ProGAN test split spans over 20 object categories (*e.g.*, *bicycle*, *bird*, *boat*, *bottle*, etc.), enabling us to examine whether the same semantic effects persist beyond face imagery. Figures 9(a, b) and 8(a–d) show the results of the naive fine-tuned CLIP. Figures 9(c, d) and 8(e–h) correspond to the fine-tuned CLIP equipped with our Geometric Semantic Decoupling module (**GSD**). In all cases, we visualize t-SNE projections of the resulting feature representations under two complementary colorings: **forgery labels** (real/fake) and **semantic labels** (face identities for facial datasets; object categories for ProGAN and CycleGAN). We observe that:

(i) **Feature collapse with naive fine-tuning across faces and natural images.** For naively fine-tuned CLIP, the more challenging settings (DFDC and FSGAN) exhibit a pronounced *semantic re-aggregation* of fake samples (highlighted by the **green circles**): fake examples form conspicuous **semantic clusters** that are not aligned with the binary decision boundary. As a result, the feature space shows substantially larger **real/fake overlap**, consistent with degraded detection accuracy under distribution shifts. A similar trend is also observed on ProGAN, where embeddings remain strongly **category-driven** and exhibit noticeable real/fake mixing near the interface between the two groups. This behavior echoes Observation I and II: when forensic cues are weak or mismatched, the representation tends to fall back to pre-trained semantic structure, undermining separability.

(ii) **GSD promotes semantic separation across faces and natural images.** In contrast, CLIP augmented with GSD produces embeddings with clearly **semantic-disentangled** cluster structure on both ProGAN and the facial deepfake datasets (DFDC/FSGAN). Specifically, forged samples no longer collapse into tight identity/category manifolds; instead, they exhibit forgery-variant organization that improves real/fake separability. This indicates that GSD encourages CLIP to encode discriminative artifacts beyond semantic content, and further suggests that semantic removal is **domain-agnostic**: it benefits both **face-based manipulations** and **natural-image generation** scenarios. The improved binary separation in the t-SNE space is also consistent with the stronger quantitative performance on forgery detection after semantic decoupling.

(iii) **Hard examples remain semantically entangled.** Finally, samples near the decision boundary or misclassified cases (highlighted by the **red circles**) consistently form highly cohesive **semantic clusters** in the identity/category-colored views. Importantly, a similar pattern can still be observed for a small fraction of samples even with GSD (*e.g.*, Figure 8(h)). This directly supports Observation III: when the forged instance is semantically almost indistinguishable from its real counterpart, strong semantic consistency can still overshadow subtle forensic evidence, making these samples intrinsically difficult.

Overall, the observations in Figure 9 and Figure 8 provide strong supplementary evidence for Observations I–III: naive fine-tuning is vulnerable to semantic fallback under shifts, while GSD consistently promotes semantic disentanglement and more robust forgery discrimination across both facial and natural-image domains.

## F.2. Attention Map Visualization

To further validate the universality of our conclusion in Section 4.4, we extend the attention-map analysis to additional and more diverse settings, including **face swapping** on FaceForensics++ (in domain, Figure 10), FSGAN (cross-manipulation, Figure 11), and Celeb-DF v2 (cross-dataset, Figure 12), as well as **full-image synthesis** on ProGAN (Figure 13). All attention maps are extracted from the [CLS] token in the last Transformer block. Across all these settings, we observe consistent trends.

(1) **Persistent attention collapse in baselines.** Both the frozen pretrained CLIP and the naively fine-tuned CLIP exhibit severe attention collapse, producing sparse single-pixel hotspots with highly similar patterns across inputs. This indicates that fine-tuning alone does not substantially alter the underlying attention behavior and can lead to a semantic fallback to

strong pretrained semantic priors.

**(2) Forensic-oriented redistribution with GSD.** In contrast, CLIP equipped with GSD consistently redistributes attention toward regions that are more plausibly forensic-relevant. On the three face-swapping datasets, GSD shifts attention from semantic hotspots to the swapped-face region and blending edges, highlighting manipulation-prone areas without any pixel-level supervision. On ProGAN, attention on real images concentrates on texture-rich structures such as object boundaries that are informative for detecting compositing artifacts, while for fake samples it becomes markedly less localized and spreads across much of the image, consistent with global synthesis.

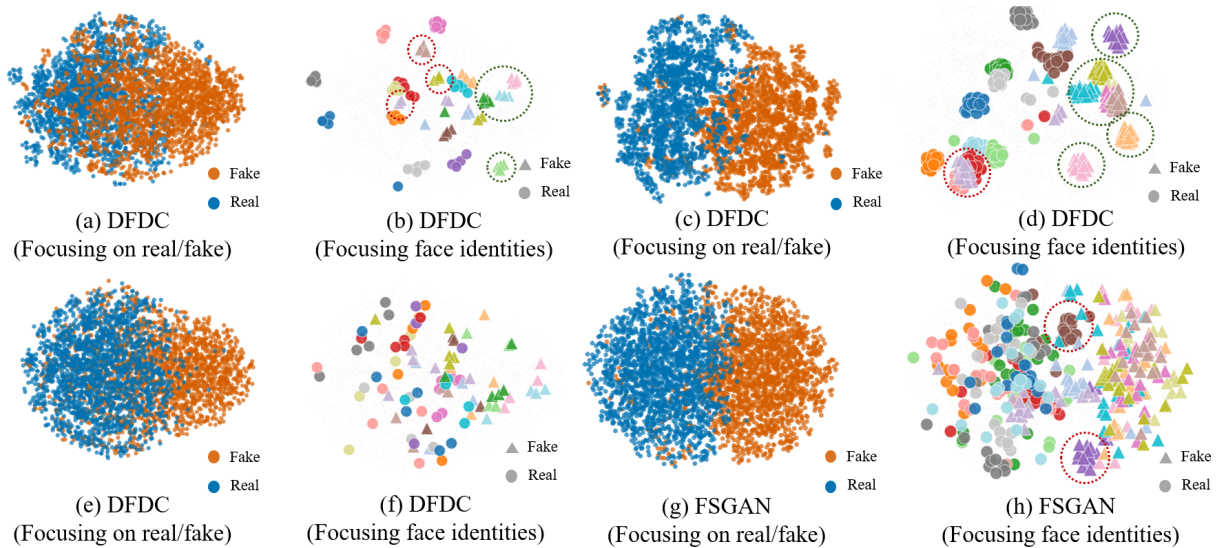


Figure 8. t-SNE (Maaten & Hinton, 2008) visualization of feature distributions extracted by the fine-tuned CLIP (a-d) and GSD-CLIP (e-h) on cross-domain (CelebDF-v2) and cross-manipulation (FSGAN) datasets. Points are colored by forgery labels (a, c, e, g) and face identities (b, d, f, h); only 20 identities for clarity.

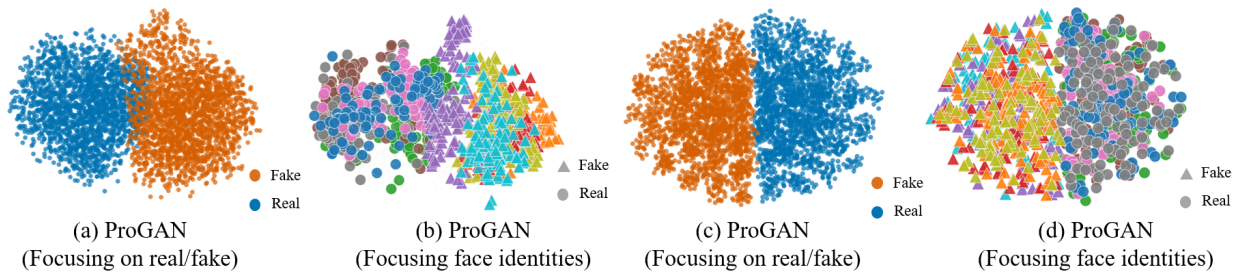


Figure 9. t-SNE (Maaten & Hinton, 2008) visualization of feature distributions extracted by the fine-tuned CLIP (a,b) and GSD-CLIP (c,d) on the ProGAN dataset. Points are colored by forgery labels (a, c) and semantic labels (b, d); only 10 identities for clarity.

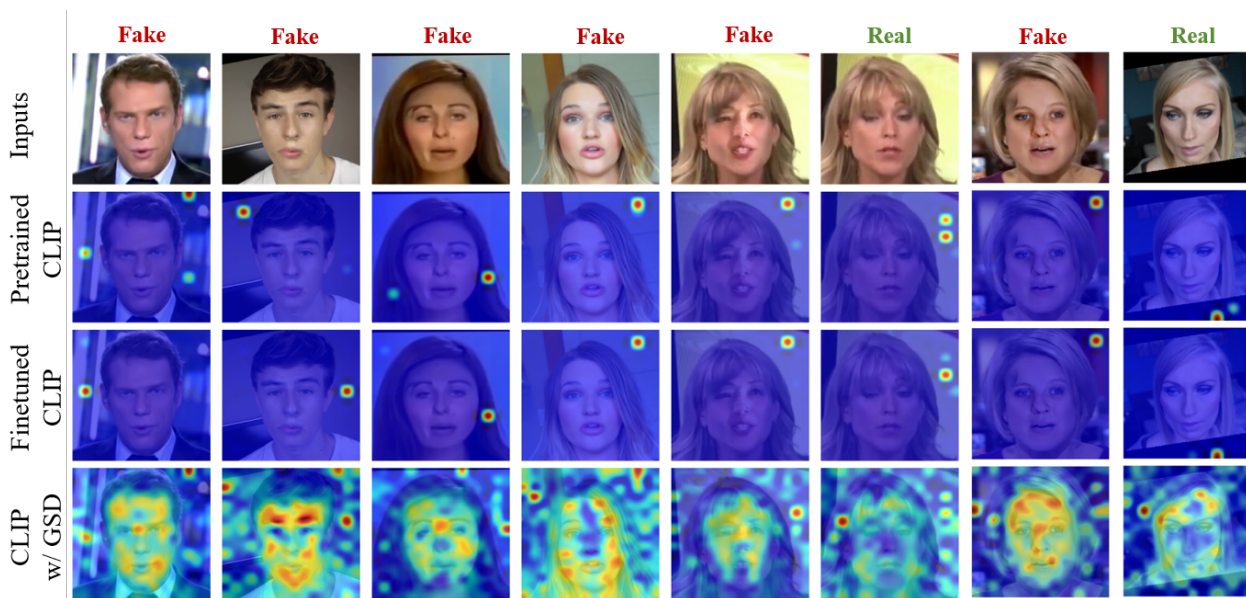


Figure 10. Attention map visualization of FaceForensics++. The top row displays the input faces, including both real and fake samples. Rows 2 and 3 present the attention maps generated by the pretrained CLIP and naively finetuned CLIP baselines, respectively. Row 4 shows the results of our proposed CLIP w/ GSD. All maps are extracted from the last Transformer block.

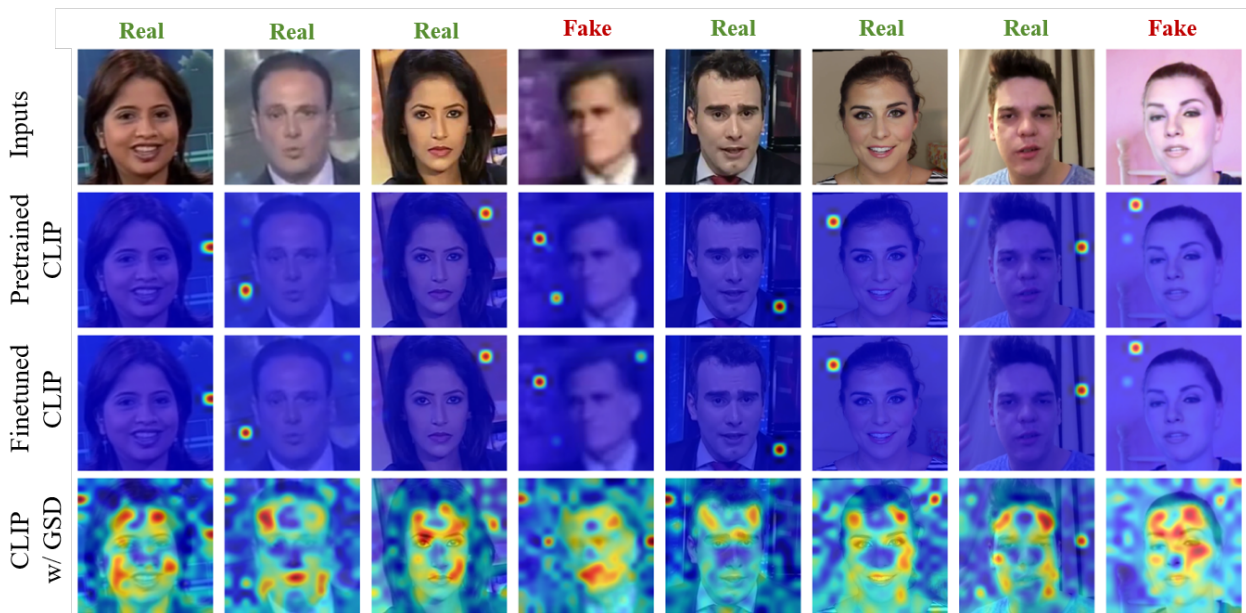


Figure 11. Attention map visualization of FSGAN. The naively fine-tuned CLIP exhibits nearly the *same* collapsed hotspot patterns as the frozen pretrained CLIP. After integrating GSD, the attention distribution becomes more aligned with manipulation-related cues: for real samples, attention concentrates around blending edges that are informative for detecting compositing artifacts; for fake samples, attention shifts to cover the swapped-face region.

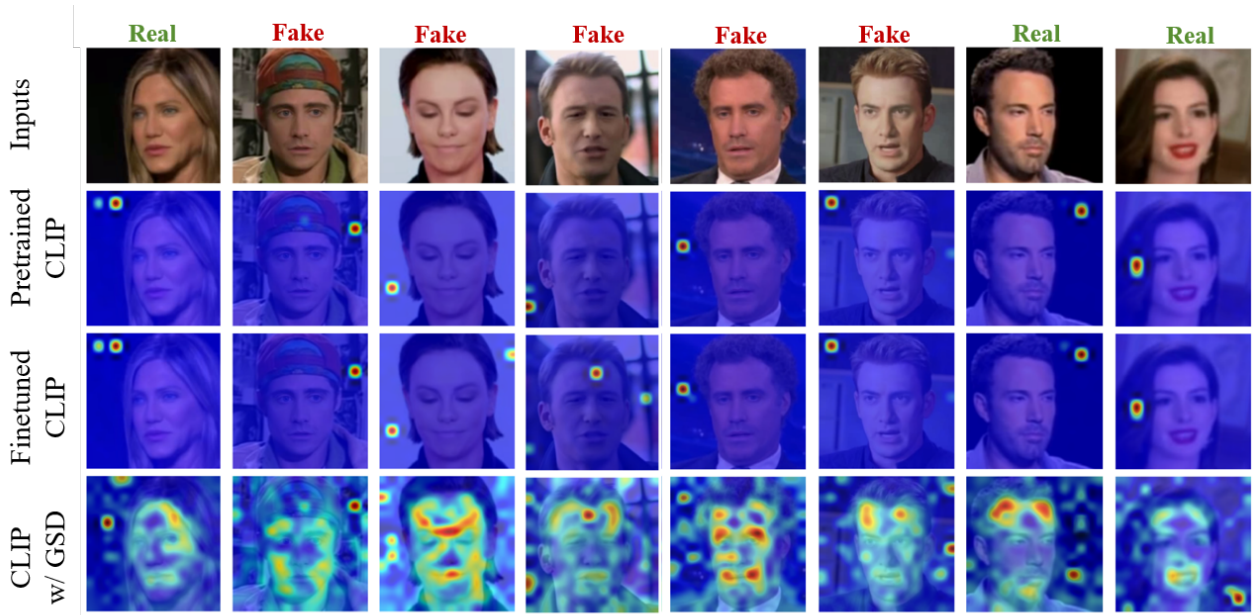


Figure 12. Attention map visualization of CDF-v2.

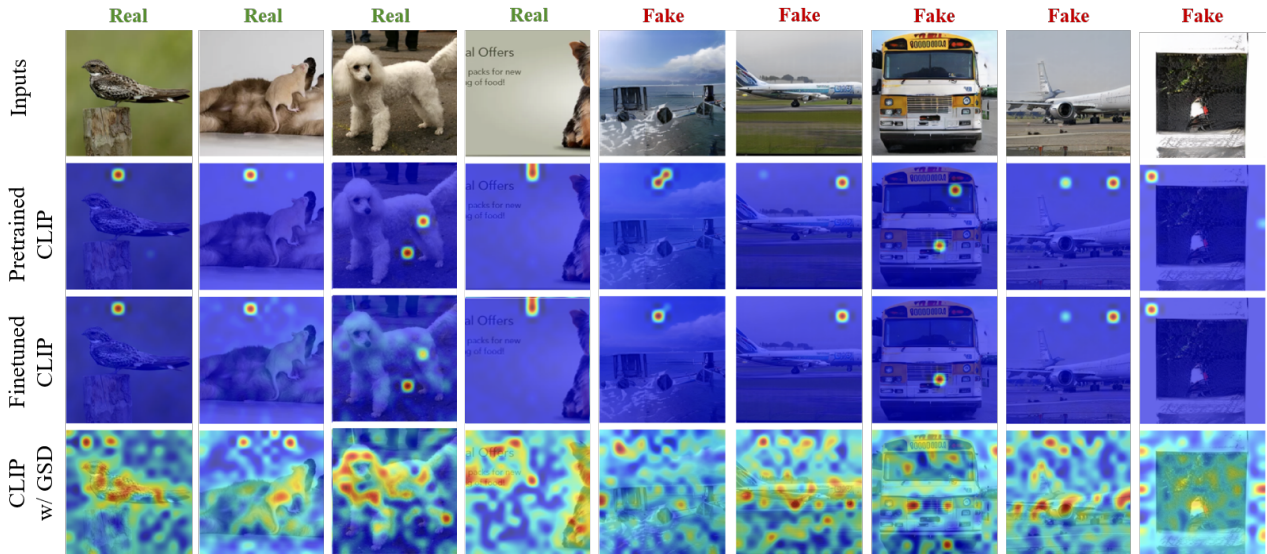


Figure 13. Attention map visualization of ProGAN. For **real** images, attention tends to concentrate on texture-rich regions, such as object boundaries and fine-grained structures; for fake images, the attention becomes markedly less localized and diffuses across the image, consistent with the fact that synthesis artifacts are distributed globally when the whole image is generated.